Technische Universität München
Fakultät für Physik

**Abschlussarbeit im Bachelorstudiengang Physik**

# Development of a fully-automated calibration system for IceCube Upgrade flasher instrumentation

**Entwicklung eines vollautomatisiertem Kalibrirungssystems für IceCube Upgrade Lichtpulser**

Leonard Geilen

September 20, 2019

Erstgutachter (Themensteller): Prof. Dr. E. Resconi
Zweitgutachter: Prof. Dr. S. Paul

## Abstract

The IceCube Neutrino Observatory is a cubic kilometer sized neutrino telescope located at the geographic South Pole. To expand its capabilities to lower energy neutrinos a major upgrade is planed during the 2022/2023 polar summer. Our institute contributes a newly developed in-situ self-calibrating flasher module (POCAM) to improve IceCube's calibration capabilities. As a total of 30 modules will be build it has become necessary to streamline production and predeployment characterization. The scope of this thesis is the development and testing of a fully-automated calibration setup able to conduct a substantial portion of the required characterization tasks. At the current state the setup can measure the changes in pulse intensity, time profile and spectrum in dependence with a change in flasher bias voltage. Six LEDs have been analyzed to determine their usability in the POCAM flasher circuit.

# Contents

# Chapter 1

# Introduction

## 1.1 Neutrino Astronomy

### 1.1.1 Neutrino

Neutrinos are leptonic elementary particles in the *standard model* (SM) with unique properties which make them ideal messenger particles for cosmic high energy events. Neutrinos neither posses an electric nor a color charge and interact solely via gravity and the weak nuclear force. As a result they have an extremely low interaction probability with other particles making even solid matter transparent to them. Opposed to photons, they can therefore cover vast distances without being scattered or absorbed keeping their energy and direction information from the point of production. Neutrinos exist in three different flavors, namely as electron ($\nu_e$), muon ($\nu_\mu$) or tau neutrino ($\nu_\tau$).

Due to the observation of neutrino oscillations one is sure neutrinos have mass. Oscillation meaning in this case that they can spontaneously change their leptonic flavor with an oscillating probability dependent on the squared mass differences between two mass eigenstates [1].

$$P_{\nu_e \to \nu_\mu} = \sin^2\left(\frac{1}{4}\frac{\Delta m_{21}^2 c^4}{\hbar c}\frac{L}{pc}\right) \tag{1.1}$$

Determining the exact neutrino mass is the subject of contemporary research with the current measured upper limit of $m \leq 0.120\,\mathrm{eV}$ [2]. This means that their mass is so small that all detectable neutrinos are super relativistic and there energy can be approximated as purely kinetic [3].

### 1.1.2 Sources

Neutrinos can be produced by hadronic and leptronic reaction in which the weak nuclear force is involved. With the main not menmade sources being $\beta$-decay, earth upper atmosphere, the sun and most interestingly for astronomers neutrinos arriving outside our solar system.

**$\beta$-decay** is a natural source of neutrinos due to decays of radioactive elements. This process exists in two variants, namely the $\beta^+$- and $\beta^-$-decay where either a proton decays into a neutron, positron and electron neutrino, or a neutron decays into a proton, electron an anti-electron neutrino.

$$p \to n + e^+ + \nu_e \qquad\qquad n \to p + e^- + \bar{\nu}_e \tag{1.2}$$

It was this process which lead Wolfgang Pauli to theorize the particle in 1930. As it posed a possible explanation for the continuous energy spectrum of the decay products. If the $\beta$-decay would only be a two particle decay, they would have to be emitted back-to-back in order to conserve momentum. This however would also determine the amount of kinetic energy each particle receives. In order to conserve momentum in a continuous kinetic energy spectrum, the momentum has to be divided up on at least three particles [1].

The discovery of the electron neutrino followed in 1956 by Cowan and Reines. They made use of the inverse process, seen in eq. (1.3), capturing anti-neutrinos created in a nuclear reactor and detecting the resulting positrons[4].

$$\bar{\nu}_e + p \rightarrow n + e^+ \tag{1.3}$$

**Atmospheric Neutrinos** are produced by cosmic rays made up of highly energetic protons and heavier atomic cores, which react with the upper atmosphere and create amongst other particles pions. These decay into muons and neutrinos. The muons in turn decay into more neutrinos as well as electrons or positrons.

$$\pi \rightarrow \mu + \nu_\mu \tag{1.4}$$
$$\mu \rightarrow \nu_\mu + e + \nu_e \tag{1.5}$$

The resulting neutrinos have energies from 100MeV to 150GeV and are therefore difficult to distinguish from other neutrino interactions or even high energy moun tracks. Mouns in particular are inherently difficult to shield and can kilometers deep into rock or ice. These particles are responsible for the most of the non-astrophysical background in detectors [1].

**Solar neutrinos** are created through various processes during the fusion reaction inside the sun's core. The most being produced during the pp-Chain reaction. It gives rise to a diverse energy spectrum with sharp energy lines from two-particle reactions such as $p + e^- + p \rightarrow d + \nu_e$ and continues spectra in the case of more than two particles being produced, like in $p + p \rightarrow d + e^+ + \nu_e$. These neutrinos posses a maximum energy of 18.77 MeV, and an average energy of 0.3 MeV [1].

**Astrophysical neutrinos** remain the great unknown. Apart from measuring a diffuse flux of high energy neutrinos [5], one only assumes that neutrino producing reaction occur in highly energetic cosmic events. With prime candidates being *active glactic nuclei*, *gamma-ray bursts, starburst galaxies, galaxy clusters* and *supernova remnants* as well as *pulsar wind nebulae*. However, to this day there are only two confirmed sources, namely the *1987A supernova* [6] and more recently the *2017A TXS Blazar* by IceCube [7].

### 1.1.3 Detection Mechanisms

The detection principle of many neutrino experiments relies on optical instrumentation looking for Cherenkov radiation produced by secondary particles of neutrino reactions. Cherenkov radiation occurs when a charged particle is traveling faster than the speed of light in the medium it is in, however it is still slower than vacuum speed of light at all times. Charged particles polarize the medium which they are traveling through but in this case the particle is so fast that the medium does not depolarize directly behind it. This delayed depolarization will result in light being emitted. One can imagine this as the particle trailing a cone of light behind it. Whose opening angle is on the particle's speed $\beta = v/c_0$ as fraction of the vacuum speed of light and the refraction index of the medium.

$$c_n = \frac{c_0}{n} \tag{1.6}$$

$$\cos(\theta) = \frac{1}{\beta n} \quad ; \beta = \frac{v}{c_0} \tag{1.7}$$

For relativistic particles $\beta \approx 1$ and eq. (1.7) simplifies to $\theta = \arccos\left(\frac{1}{n}\right) = 41°$ if one uses a refraction index $n = 1.31$ for ice.

Generally speaking Cherenkov spectra are continuous and independent from the energy of relativistic particles. The particles energy only the length of the track is determined by the particle energy and therefore integrated light intensity of the entire track. As the main part of the spectrum is within the deep UV range, only particles over a certain energy threshold have a high enough intensity to create a measurable amount of photons in the visible range [8].

The underlying weak interactions, creating charged particles in a detector volume can be classified in *neutral* (NC) and *charged currents* (CC). In NC the $Z^0$ boson mediates the interaction force, in CC the electrically positively charge $W^+$ or the negative $W^-$ boson. The most typical reactions, namely Neutrino absorption, Pair annihilation, Muon decay and the $\beta$-decay being depicted as Feynman graphs in fig. 1.1.

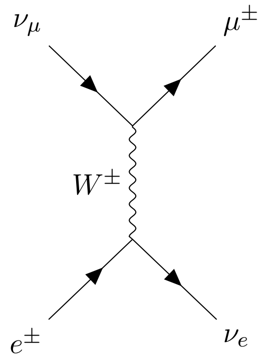


**(a)** Neutrino absorption (CC), $\nu_\mu e^\pm \to \mu^\pm \nu_e$

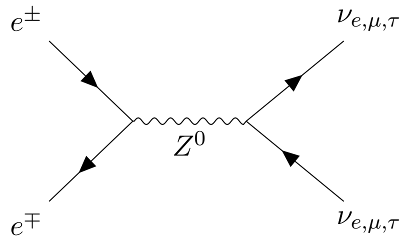


**(b)** Pair annihilation (NC), $e^\pm e^\mp \to \nu\nu$

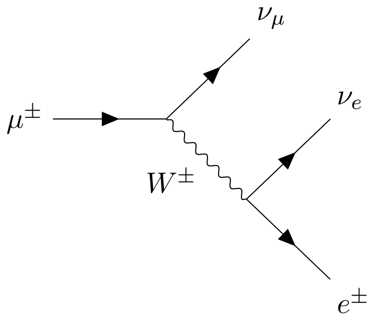


**(c)** Muon decay (CC), $\mu_\pm \to e^\pm \neq_e \nu_\mu$

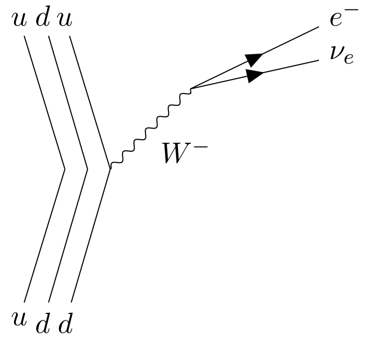


**(d)** nuclear $\beta^-$ decay (CC), $n \to p^+ e^- \nu_e$

**Figure 1.1:** A selection of Feynman diagrams with charged and neutral current neutrino reactions. The most interesting reactions for neutrino astronomy are the absorption and the pair annihilation, as it also describes neutral current scattering if rotated by 90°[9].

As astrophysical neutrinos have extremely high energies their scattering inside the detector medium is deeply inelastic, producing cascades of secondary and tertiary particles. Here mostly Apart from Cherenkov light, these particles also produce further photons through bremstrahlung, pair production and annihilation [1]. In order to observe the complete cascades and to have a reasonably high probability of neutrino interactions large detector volumes are chosen [3].

## 1.2 IceCube Neutrino Observatory

### 1.2.1 Detector

One example of a currently-operated Neutrino Observatories is IceCube. IceCube, located at the South Pole, instruments around one cubic kilometer of Antarctic ice with a sensor array dedicated to high-energy neutrino detection.

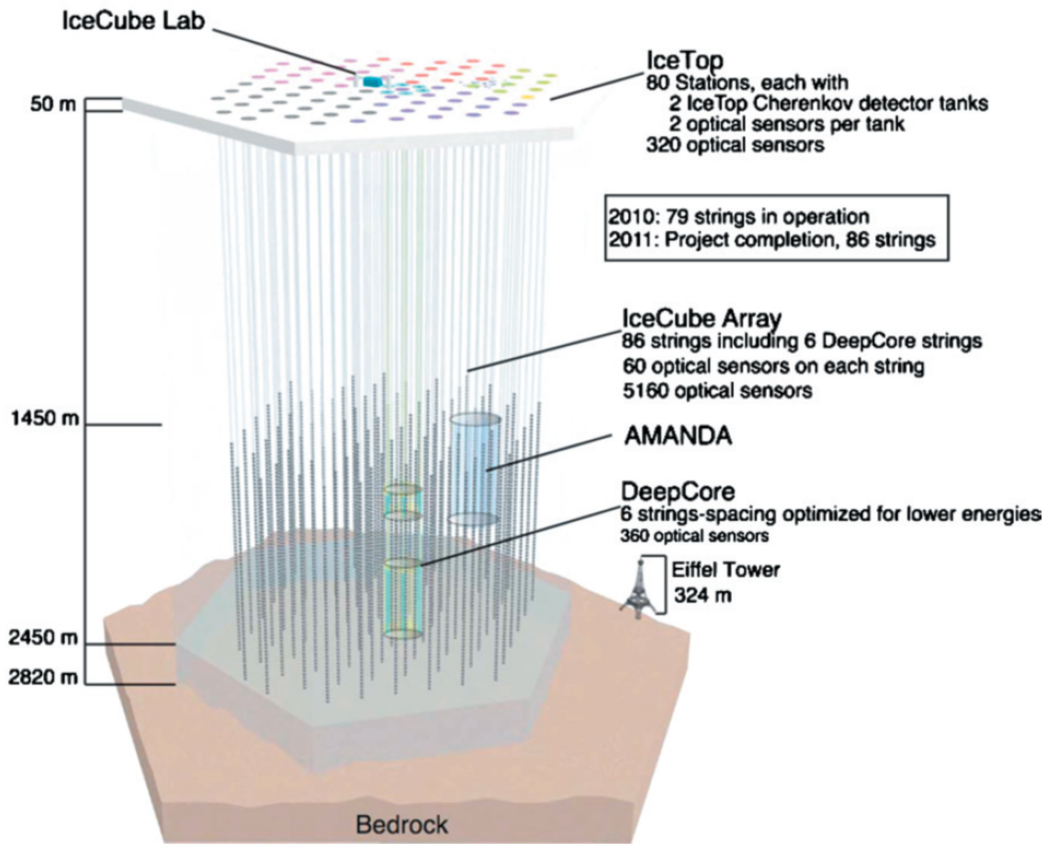


**Figure 1.2:** The render shows the current state of the IceCube neutrino detector with 86 strings being deployed in a hexagonal shape and a detection volume of about one cubic kilometer. The DOMs original belonging to AMANDA and those of the deep core array are highlighted [10].

After success of its predecessor project AMANDA [11] it was decided to expand the operation to now 86 string with a total of 5160 optical sensors. These sensors instrument the ice at depths between 1450 m and 2450 m. On 80 of strings the individual measurement modules are spaced 17 m apart vertically and the strings are 125m horizontally into a hexagonal shape. The remaining 6 strings are more closely packed in the center and make up the so called *deep core* array. An additional 320 detectors are frozen into water tanks at the surface to detect cosmic ray showers and veto possible atmospheric muons.

The sensors are so called *digital optical modules* (DOMs) and consist of a glass sphere with the lower hemisphere being filled by a 10" photo multiplier (PMT) and the upper with the read out and auxiliary electronics, as well as an LED flasher board which is used for calibration purposes [12].

### 1.2.2 Calibration

The main contributors to the systematical uncertainty in the reconstruction of IceCube events are the not fully understood scattering and absorption properties of the ice, as well as ice impurities and angular acceptance and detection efficiencies of the DOMs. Together these effects amount to a systematical error of 10% [13].

As South Pole ice is a naturally grown product, absorption and scattering length vary dependent on the depth [3]. This for example destroys the shape of Cherenkov cones produced in the Ice. The DOMs using photo multiplier to measure the light intensity, have a varying efficiency for different wavelength. Further more as the exact orientation of the modules in the ice can not yet be measured precisely, direction-dependent effects like total reflection at the DOM glass sphere can not be established in detail. To further reduce the systematical errors well-characterized light sources are used to fit calibration parameters from the measured detector response. For this especially the knowledge of the light sources pulse intensity, spectrum and time profile is of importance [3].

### 1.2.3 IceCube Upgrade (ICU)

For 2022/2023 arctic summer the IceCube Collaboration is planning a major upgrade to the detector, mainly to boost low energy resolution for neutrinos at energies of a few GeV [14]. This will improve especially the reconstruction of atmospheric neutrino events and and use them for precision studies of low-energy neutrino physics, e.g. neutrino oscillation parameters.

In practice this translates to seven new strings within the so called *physics region* of IceCube. A region at the center bottom of the detector in depth of $2150 - 2450$m with particularly clear ice and good shielding from atmospheric muons and photons. The strings will be placed with 20 m horizontal spacing with modules attached in a 3 m interval along each string. Certain specialized modules will extent above and below the physics region. There purpose being either to improve veto of background or calibration.

Most modules will be upgraded versions of the existing DOMs with 5ns (FWHM) LED flashers, CCD cameras, pressure, temperature, magnetic field and orientation sensors. Other being testing Hardware for IceCube-Gen2. Or as is the case for the *Precision Optical Calibration Module* POCAM a standalone light emitting module for in-situ ice calibration and detector response measurements [15]. The resulting newly established calibration data can also be used for event reconstruction in archived IceCube data from the last decade [14].

## 1.3 Semiconductors

### 1.3.1 Metals, Insulators and Semiconductors

In solid state physics one categorizes the electronic properties of materials into insulators, conductors and semiconductors. This classification is based on the electronic band structure of crystalline materials. Electronic bands represent the kinetic energy states, which electrons can occupy. Due to the Pauli exclusion principle only one electron is allowed to occupy a given energy state. Therefore the bands are only quasi-continuous as there is a minimal energy step between the states. The fact that the energy states are not one single band but multiple bands with band gaps, meaning an absents of states, in between is due to way they are formed. In essence the principle is the same as in any molecule with the overlapping wave functions of the electron orbitals forming new molecule orbitals with bonding and anti-bonding properties which are then occupied by the shared electrons. The main types of bonds are the sigma (s-like orbitals) and the pi bonds (formed from p-like orbitals). Due to the shear number of electrons in a crystal these bonds widen into the bands [16].

The same way that electrons are localized in a sigma bond between the two interacting atoms, they are localized as well in the corresponding s-like band, making it non conductive. This band is typically formed by the valence electrons of the individual atoms and therefore called valance band.In contrast electrons in pi-bonds can be localized over multiple atoms or even the entire molecule. Meaning that they are delocalized in their corresponding band as well, which is therefore conducting. Accordingly the band is called the conduction band. Mathematically the filling of the bands with electrons can be described by the Fermi-Dirac distribution which takes the Pauli exclusion principle into account.

$$\bar{\mathcal{N}}(\varepsilon) = \frac{g(\varepsilon)}{e^{(\varepsilon-\mu)/k_B T} + 1} \tag{1.8}$$

Here $\bar{\mathcal{N}}(\varepsilon)$ is the average number of occupied states at the energy $\varepsilon$, with $g(\varepsilon)$ being the Density of State at the energy, $\mu$ being the chemical potential of the crystal and $k_B T$ the thermal energy. In the limit of temperature towards zero kelvin the distribution becomes a step function meaning that even in the absence of thermal energy only one electron occupies the ground state and from thereon higher energy states are filled successively. At higher temperatures electrons at the edge of the step have a high enough kinetic energy to jump into higher states close by and the step softens [17].

The highest occupied state defines the so called Fermi energy or Fermi level. As these are the electrons that most probably can jump into the next higher states, the position of the Fermi level in the band structure of a crystal greatly determines its electrical properties. It is important to note that due to the lack of unoccupied states, filled bands do also not conduct. This leads to the afore mentioned categorization into conductors, semiconductors and insulators.

In a conductor the Fermi level lies within the conduction band and therefore free moving electrons are present in the crystal at all times making them permanently conductive as is the case for all metals. In a semiconductor the Fermi level lies in between the valence and the conduction band. As long as the band gap is not to large electrons can be exited into the conduction band. This makes the conductivity of the crystal switchable. In contrast to that the energy gap in an insulator is to large to excite a macroscopic number of electrons into the conduction band making them non conductive. Excitation of electrons into higher states can happen through a variety of different process, most importantly through the absorption of photons. The excited electron leaves a hole in the valence band, which can be interpreted as a positively charged quasi-particle. In contrast to electrons it can move in the valence band due to its high positional uncertainty although at a slower speed than the electron in the conduction band [18].

### 1.3.2 P-N-Junction

A very effective way to modulate the Fermi level in a semiconductor is the process of doping. Here one intentionally introduces impurities into the crystal. Typically these impurities are atoms from neighboring main groups in the periodic system. If the impurity atom has one valance electron to much it will remain loosely bound to the impurity will in effect become a free moving electron at room temperature, therefore increasing the amount of free electron states and therefore shifting the Fermi level closer to the valence band edge. In the alternative case of the impurity atom having a valance electron to few a vacant bond is introduced into the crystal and therefore the number of free holes increased. This shifts the Fermi level towards the conduction band edge. As the former increases the amount of free negative charge carriers it is called n-doping and the later, increasing the amount of positive holes, p-doping. In both cases the semiconductor remains electrically neutral as the introduced ions carry the opposite charge to the introduced carriers.

If a p-doped and a n-doped crystal are broad into contact the result is a p-n-junction. At the interface a portion of free holes from the p-doped region will diffuse into n-doped region and recombine with the free electron there. Like wise will a portion of free electrons from the n-doped region recombine in the p-doped region. The result is a region around the interface with no remaining mobile charge carriers and as the recombined carriers leave behind immobile ionized impurities an electric field is formed stopping further electrons and holes from entering the depletion region.

As soon as an equilibrium state is reached the Fermi levels of both regions are identical. Under the assumption a that all dopants are ionized and therefore the free electron density $e = N_D$ equals the donor density and the free hole density $p = N_A$ equals the acceptor density the following equation for the *diffuse voltage* holds true:

$$V_D = \frac{k_B T}{e} \ln\left(\frac{N_A N_D}{n_i^2}\right) \tag{1.9}$$

With $n_i^2$ being the free carrier density in the undoped *intrinsic* semiconductor. If one connect electric terminals to the p- and n-doped sides one have effectively build a simple diode. A diode is an electric device whose resistance varies extremely from the polarity of the applied voltage. In the case of the negative pole being connected to the p-doped region and the positive pole being connected to the n-doped region on speaks of a *reverse bias.*

In this case electrons are injected into the p-doped region where they will recombine with the free holes, effectively reducing there concentration. The opposite is happening in the n-doped region where the free electrons combine with the injected holes. As both the number of free electrons and holes is reduced the remaining free carriers are pulled away from the depletion region and therefore enlarging it. This has the effect of increasing the internal electric field which is opposite to the externally applied field. As a result the diode behaves as an insulator upto a certain breakdown voltage, at which point the external field is big enough to over come even if the entire diode is depleted.

In *forward bias* the negative pole is connected to the n-doped region and the positive to the p-doped. As the injected free electrons can move freely in the n-doped region and the injected holes in the p-doped region respectively they both arrive at the depletion region recombining first with the diffused holes and electron eliminating the opposing electric field and later with each other closing the electric circuit.

The behavior of the current in an ideal diode dependent on temperature $T$ and bias voltage $V$ as well as semiconductor specific variables is given by eq. (1.10):

$$I = eA\left(\sqrt{\frac{D_p}{\tau_p}}\frac{n_i^2}{N_D} + \sqrt{\frac{D_n}{\tau_n}}\frac{n_i^2}{N_A}\right)\left(e^{eV/k_B T} - 1\right) \tag{1.10}$$

$D_n$ and $D_p$ are electron and hole diffusion constants, $\tau_n$ and $tau_p$ minority carrier life times, $N_D$ and $N_A$ donor and acceptor dopant densities and $n_i^2$ being the free carrier density of the undoped crystal and $A$ the cross-sectional area.

Simplified formulas for forward biased and reverse biased diodes exist, with:

$$I = I_S \left( e^{eV/k_B T} - 1 \right) \tag{1.11}$$

with $I_S$ being the saturation current which is equal to the prefactor of eq. (1.10), but also can be determined experimentally.

In the case of a forward bias one can make the assumption that $\exp(eV/k_B T) - 1 \approx \exp(eV/k_B T)$ as the applied voltage $V \gg k_B T/e$, the result is:

$$I = eA \left( \sqrt{\frac{D_p}{\tau_p}} N_A + \sqrt{\frac{D_n}{\tau_n}} N_D \right) \mathrm{e}^{e(V - V_D)/k_B T} \tag{1.12}$$

With $V_D$ representing the threshold voltage for conduction to occur [19].

### 1.3.3 Light Emitting Diodes (LEDs)

In essence a LED is p-n-junction optimized to radiatively recombine when a forward biased voltage is applied. This means that mostly direct semiconductors qualify for the production of LEDs. In a direct semiconductor only a one componential wave vector is required to convey the energy difference between the conduction band minimum and the valence band maximum. As opposed to an indirect semiconductor where a two componential vektor is needed. As photons have only have a single componential wavevector an optical transition in an indirect semiconductor would have to rely on lattice vibrations to convey the other impulse component making it in fact a three particle reaction and therefore much more unlikely.

In an direct semiconductor the energy of its emitted photons is equal to the band gap. This only changes at very high injection of electrons and holes. In this case all energy states close to the band edges are in use and energy transitions from states deeper in the conduction and valance band become more probable. This shifts the spectrum towards higher energies thus shorter wavelengths.

The wavelength is therefore mainly dependent on used the semiconductor material. This makes the development of LEDs in certain wavelength regions extremely complex as most semiconductor have a band gap corresponding to a red or infrared wavelength. Most blue and UV LEDs require some sort of artificially grown semiconductor structure to form a quantum well. In the green spectral region a combination is used as for example in gallium phosphate semiconductors where an Nitrogen impurities are used to achieve a radiative transition.

To increase light yield most LEDs are encapsuled in a Epoxy resin. This is due to the fact that most crystals have extremely high refraction indices making total reflection at a crystal air interface very likely. The Epoxy has a refraction index in between that of a typical crystal and air, this makes for two less extreme transitions in optical density and overall reduces total refraction. Furthermore the light yield can be increased by geometrical optimization of the LED and positioning of the semiconductor.

The Epoxy is also one of the reasons that light intensity of an LED decreases over time, as especially shorter wavelength LEDs can break down the Epoxy polymer. The semiconductor it self can loose efficiency over time to as the high temperatures reached during continuous operation. These encourage certain reactions in the semiconductor resulting unwanted impurities or permanently conducting surfaces [19].

# Chapter 2

# POCaS

## 2.1 Precision Optical Calibration Module (POCAM)

The contribution from our institute to the IceCube Upgrade is the *Precision Optical Calibration Module* (POCAM). It is a standalone module capable of producing well-characterized, isotropic light pulses with absolute intensity calibration. Once deployed, these can be used as a reference for calibrating detector response as well as quantifying and improving systematic uncertainties in the Antarctic ice.

To be of value for calibration, the module was designed to handle the following requirements: First it must be able to cope with the environment present at the South Pole, i.e. temperatures of around $-40\,°C$ and high pressures upto 700 bar. Especially as drilling leaves liquid water in the drill hole left to refreeze after deployment finished, hydrostatic pressure can peak far above what would be expected from the water depth alone. Secondly, the light pulse properties have to be well determined and controlled in order to provide clear signals within the instrumented detector volume. This means primarily that they should be similar to astrophysical neutrino event signatures in terms of brightness and timing. In order to avoid inhomogeneities in these light pulse signatures, the POCAM makes use of semi-transparent integrating spheres which enable the light emission to be isotropic in 4
*pi*. Furthermore the wavelength range of each individual pulse should be well-known but simultaneously the module should cover the $300 - 600$nm range to which IceCube DOMs are most sensitive [15]. And third, the module has to be integrated into the complex IceCube data acquisition system [20] while still maintaining calibration independence of the detector. For the latter, the POCAM makes use of integrated sensors to monitor light intensity, pulse on-set timing as well as orientation and environmental data. Together with the fingerprint-characterization versus various parameters, this will provide an independent and well-characterized light source in the detector volume which can be used for detailed detector studies.

### 2.1.1 Module

To meet all these requirements, the following design has been developed: A spherical module would be the best choice to isotropically emit light, but as all supporting electronics would have to be housed inside the light source to not cast shadows it is difficult to realize [21]. Therefore, a cylindrical shape with two hemispheres at the end has been chosen [15]. This allows each hemisphere to emit with almost 2
*pi* with all of the necessary electronics housed inside the cylinder out of the field-of-view.

With a length of 40 cm it is still possible to approximate the module as a point source from typical IceCube distances.

To cope with the environmental conditions the cylinder is made out of titanium and the glass hemispheres are optically cleared borosilicate glass, called BK-7. Due to its thermal expansion coefficient being very similar to that of titanium the risk of thermal stress created at the material interfaces is greatly reduced.

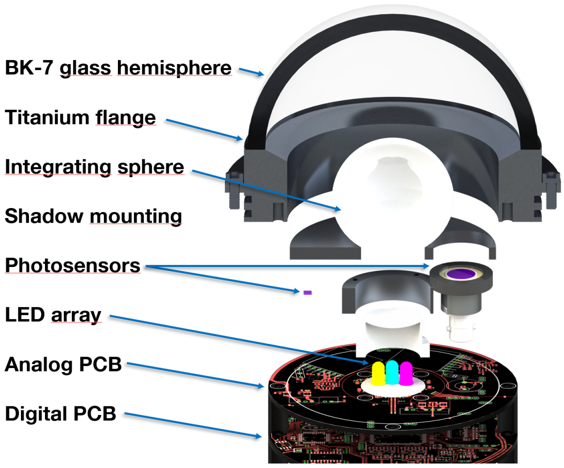


**(a)** Scematic of one of the two hemispheres of the POCAM [15]

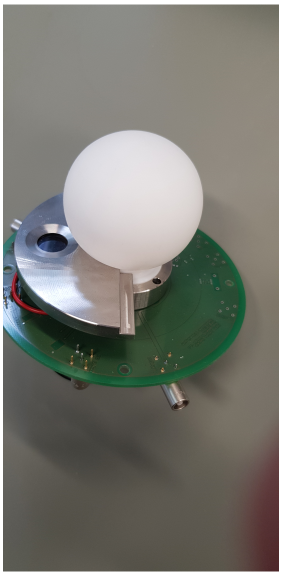

**(b)** Prototyping phase of the POCAM analog board with attached integration sphere and halve of the uncoated surface plate.

The actual sources of light are pulsed LEDs on a flasher board emitting into an integration sphere located in the center of each hemisphere. The driver circuit in combination with the chosen LEDs has to provide intense and sharp nanosecond light pulses. One of the included drivers that is capable of doing this is the circuit [22] which is discussed in detail in section 2.1.2. Although the exact LED selection is not yet finalized, up to six different wavelength LEDs can be hosted in each hemisphere. The current design foresees each hemisphere holding three different driver circuits each providing different light pulse features. So far the only 405 nm LEDs have been used for IceCube calibration, hence it is refer to as the *default LED*. Each hemisphere will contain three different pulser circuits with this LED. The remaining LEDs being selected to best cover rest of the wavelength range between 300 and 600 nm.

The integrating sphere is used to make the directional LED light emission isotropic. Here, PTFE, often marketed as Teflon has proven to be the material of choice. Although further studies have shown, that optical PTFE might be an even better choice. It is semi-reflective material which diffusely reflects part of light, entering from the LED below, while the rest is transmitted through the material. Due to the spherical shape this transmission is isotropic. As each sphere only emits 180°, the mounting plate under the integrating sphere is coated in a black to prevent scattered light from the lower surface to contribute to the light emission which would other wise decrease the isotropy.

Integrated into the mounting plate of each hemisphere is a *photo diode* and a *silicon photo multiplier* (SiPM) which gives rise to in-situ calibration capabilities. Accompanying is auxiliary electronics to read out the sensors, handle communication and supplying all necessary voltages and triggers. To determine environmental conditions in the ice, a thermometer and pressure sensor is included as well as gyroscopes and accelerometers for the position and orientation. As a mean to prevent condensation on the sensors or glass, the entire module is nitrogen flushed and evacuated to a pressure of around 0.3 bar [9].

### 2.1.2 Default Flasher

For prototyping of the setup a simpler board is used, having only one LED and a Kapustinsky driver. A schematic for the circuit can be seen in the fig. 2.2. The trigger signal is a square wave with an amplitude of 5 V provided by a signal generator connected to the board. As during testing and calibration, it is necessary to collect many samples so the trigger is set to 10 kHz significantly higher than during operation. The only other connection to the board is the negative bias voltage which is also provided by an external device.

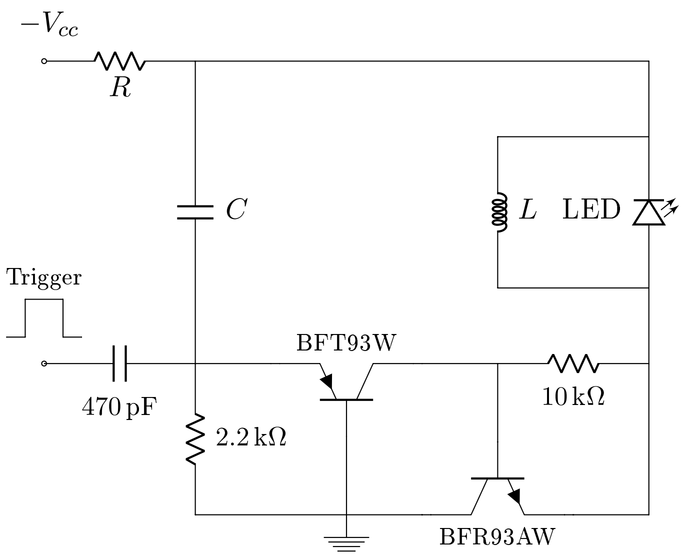


**Figure 2.2:** The Kapustinsky driver circuit is can generate nanosecond short LED pulses, with the exact characteristics determined by the capacitor C, the coil L and the LED itself. As connection a negative bias voltage $V_{cc}$ and a trigger signal is required [9].

The Kapustinsky circuit is able to produce an intense LED flash with a length of under 10 ns (FWHM) by using a self stopping LC-circuit forcing a very high current through the LED. The exact schematics can be seen in fig. 2.2. The capacitance C, inductance L and the LED its self are the elements having the most effect on the pulse shape.

As soon as the bias voltage is applied the capacitor C is charged as it has a connection to ground via the 2.2 kΩ resistor. The trigger is AC-coupled via a 470 pF capacitor and therefore will induce a potential on the emitter side of the PNP transistor (BFT93W) which switches with GHz speed. The opened transistor now allows the trigger signal to reach the gate of the PNP transistor (BFR93AW) which also opens with GHz speed. Resulting in a direct connection to ground, allowing the capacitor C to discharge over the LED.

At first the coil L in parallel to the LED has little to no effect, due its high resistance for fast changing currents caused by its inductance. During the pulse, as the current becomes stable, the capacitor will increasingly discharge via the coil as opposed to the LED. The resulting current in the coil will build up a magnetic field. As the capacitor is completely discharged and the current fades away, the magnetic field in the coil collapses and induces a reverse current. This eliminates any potential holding the NPN transistor open via the $10\,\mathrm{k\Omega}$ resistor. In effect, the LED has nomore connection to ground and the LC circuit is interrupted, giving the capacitor time to recharge, resetting the flasher for the next trigger.

### 2.1.3 Calibration Chain

One of the major advantages of the POCAM lies in the absolute calibration it receives prior to deployment and its resulting ability to monitor its light output over time.

The three properties of each pulse that are of importance for IceCube are: The total absolute intensity of each pulse, hence the amount of photons emitted, the mean wavelength of the light and the pulse time profile.

In order to create a complete calibration, the influence of all varying system parameters during operation has to be quantized. The two main controllable parameters are the bias voltage and trigger rate. During calibration in the laboratory, even environmental factors such as temperature need to be controlled. This, in combination with aging over time, are the parameters that are expected to have the most effect on the emission of the characteristics of the LEDs. The last important parameter is the orientation of the flasher module is its orientation, as it has to be verified how the light is emitted into the detector volume. The main driving reason for that is a marginal dip in intensity around the waistband region where both hemisphere emissions overlap. The knowledge of this dip orientation improves calibration precision.

All measurements have been conducted at 10 kHz which is the maximum frequency at which the Kapustinsky capacitor is still reliably fully charged [9]. This is significantly higher than during operation and has been chosen to reduce measurement time as many pulse samples need to be taken.

From all of the calibrations, the intensity calibration is the most complex as it is additionally influenced by the modules orientation. Therefore it is separated into three measurements. With the first being a relative one correlating the flasher intensity with temperature and supply voltage. The second one which is still a relative one correlating intensity to angular orientation of the flasher. And the third one determining the absolute brightness of the flasher at fixed angle and distance. This last measurement sets a fixed scale for the other two and therefore their results can becomes absolute too.

The wavelength and time profile calibrations are a little less complex and can be done in a single step, as both are independent from the orientation and absolute intensity of the flasher. The wavelength can be measured directly with a spectrometer which works by integrating the light over a set time. By adjusting this integration time the spectrometer can operate at vastly different intensities and therefore cover all the dynamic range of the POCAM. The time profile is determined by time correlated single photon counting. The principle of this process is to greatly attenuate the arriving light until only a single photon per pulse arrives at a sensor. Then, one uses a fast photosensor to measure the delay time between trigger and detector response. Instead of trying to measure a photons position at a given time one can simply measure delay time between trigger and it being detected at the sensor. By taking enough samples and binning them in time one can effectively reconstruct the arrival probability function. The underlying principle being the law of large numbers. As this probability density function is directly proportional to the intensity of the wave package it represents the shape of the pulse.

## 2.2 POCAM Calibration Station (POCaS)

### 2.2.1 System requirements

Due to the fact that IceCube collaboration has ordered 30 POCAMs [15] with two hemispheres each, it has become necessary to calibrate 60 analog flasher boards, with 6 LEDs each. The scope of this bachelor thesis is the development of a fully automated calibration station.

As discussed in section 2.1.3, it is expected that temperature and the supply voltage have a strong impact on the characteristics of the LED pulse. Therefore the setup has to precisely control both of these parameters in order to measure the change in light intensity, wavelength and pulse shape. This setup is designed to completely automate the relative intensity as well as the wavelength and time profile measurement of the calibration chain.

### 2.2.2 Setup

The calibration setup consists of two main parts, namely the fridge as an temperature-controlled environment for the LED flasher and a dark box for all optical measurements, as well as peripheral devices such as various power supplies and a computer controlling the measurement sequence and saving the data. The fridge is capable of reaching $-80\,^{\circ}\mathrm{C}$ and is therefore well-suited to simulate the temperatures at the South Pole in general and inside the IceCube detector in particular. In the final setup the fully assembled analog board will be mounted inside the fridge connected to an optical 4-to-1 fan-out fiber and is then directed through a plug in the wall of the fridge into the dark box to the measuring instruments. Due to the fact that the freezer only became fully operational shortly, all measurements have been conducted at room temperature.

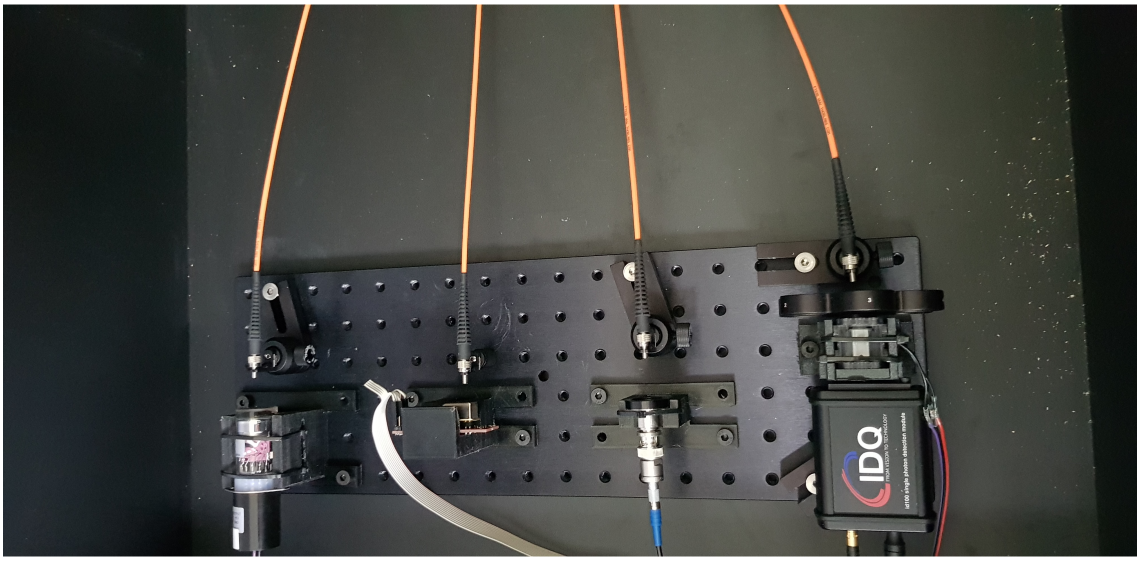


**Figure 2.3:** Picture from the instrumentation setup inside the dark box. From left to right one can see the photomultiplier, the spectrometer, the photo diode and the avalanche photo diode.

As can be seen in section 2.2.2, inside the dark box are the four main measuring instruments, namely a *photo-multiplier* (PMT), a photo diode, a spectrometer and an *avalanche photo diode* (APD). As no instrument but the spectrometer has a fiber adapter the fiber has to be aligned manually. Although this poses the risk of making the measurements less repeatable, as long as it is not touched during a measurement it is of little concern due to the relative nature the measurements at the beginning of the calibration chain. The exact instruments used are a *Hamamatsu R1925A* PMT [23], an IDQuantiqe ID100-50 APD [24], the *Hamamatsu S2188-01* photodiode [25] and a *Hamamatsu C12088MA* spectrometer [26]. The complete setup can seen in section 2.2.2.


**Figure 2.4:** Laboratory setup with the dark box in the middle, the freeze to the right and the picoamperemeter, picoscope, trigger generator, power supplies and the measurement computer in the shelf above. The second oscilloscope to the left of the dark box is only used for improvised measurements and debugging.

The photo diode and the PMT are both used to measure the pulse's intensity. The PMT is used for the low and the photo diode for high intensity range. As the photo diode produces a current proportional to the amount of photons arriving, it is connected to a picoamperemeter. This amperemeter is capable of measuring currents in the pico ampere range. It furthermore is programmable to take automatic measurements and sends the results to a the computer via serial connection. The PMT responds with self-amplified charge pulses once arriving photons have freed electrons on its photoactive area. These pulses are recorded with an oscilloscope and used for further analysis. The required high voltage to operate is created by a high-voltage generator with input from the laboratory power supply. For safety reasons all high-voltage devices are housed inside the dark box.

The spectrometer is used to measure the wavelength spectrum of the LED. It is serially connected to a single-board computer which in turn runs the measurement sequences as well as data acquisition to the main computer.

To realize the APD measurement and a filter wheel is used to attenuate the arriving intensity to single photons. The APD will produce a signal every time a photon arrives on its active surface. For later determination of the time delay both its signal and the signal of the trigger generator is recorded by the digital oscilloscope. To be reasonably certain that only one photon at a time arrives at the APD the occupancy, meaning the ratio of detected to triggered pulses, has to stay below 10%. Using the Poissanian probability distribution:

$$\mathcal{P}(k, \nu) = \frac{1}{k!} \mathrm{e}^{-\nu} \nu^k$$

where $\mathcal{P}(k, \nu)$ is the probability of $k$ photons being detected per pulse and $\nu$ the average detected number of photons. Hence the occupancy can be expressed as the probability of the number of detected photons being higher than zero. The following expression can be derived:

$$\begin{aligned} \mathrm{occ} = \mathcal{P}(k \geq 1, \nu) &= \sum_{k=1}^{\infty} \frac{1}{k!} \mathrm{e}^{-\nu} \nu^k = \mathrm{e}^{-\nu}(e^{\nu} - 1) \\ 1 - \mathrm{occ} &= e^{-\nu} \\ \nu &= -\ln(1 - \mathrm{occ}) \\ \mathcal{P}(k \leq 1, \mathrm{occ}) &= (1 - \mathrm{occ})(1 - \ln(1 - \mathrm{occ})) \end{aligned} \tag{2.1}$$

For an occupancy of 10% the resulting in a single-photon purity $\mathcal{P}(k \leq 1, \mathrm{occ})$ is 99.5%.

#### 2.2.2.1 Systematics

As the absoluteness of the measurement is paramount, possible systematical errors have to be established.

First, the wavelength measurement. It has the unique feature, that its statistical error is influenced by the systematical error. This is due to the fact that the flasher intensity influences the signal to noise ratio in the spectrometer. The spectrometer works by splitting the incoming light into its spectrum which is then projected onto a linear array of pixels. Therefore the pixel position represents the measured wavelength and the voltage created during the integration time represents the intensity of light at the pixel. The individual pixel voltages are then digitized by an Analog to Digital Converter (ADC) with the maximum value being $2^{15}$. As the pixels are sensitive to thermal radiation, the ADC range will slowly by filled even if no photons from the flasher arrive. A test measurement is conducted before every measurement run to determine this dark rate and, depending on the room temperature, it takes between 6 s to 7 s before halve of the ADC range is saturated by noise. As not all pixel saturate equally fast before every illuminated measurement a dark measurement is conducted, with the difference of the two signals being the measured spectrum.

The statistical error for every pixel is given by $\sqrt{N}$ with N being the counts. One can now see that for very low intensities the remaining ADC range after the dark count is subtracted is significantly smaller than for high intensities where the integration time can be chosen very small. In effect this makes the Gaussian fit of the mean wavelength less accurate. The second and probable dominant systematic is the calibration of pixel channel number to wavelength. The function is a fifth order polynomial given by the manufacturer Hamamatsu. The spectral resolution is only 12 nm (FWHM) with a reproducebility of ±0.5 nm [26]. Due to the fact that the other instruments, outside of the freezer, are at room temperature and shielded from direct sunlight by the dark box. Furthermore is the laboratory room climate controlled making extreme temperatures unlikely. As the freezer's temperature is varied to observe LED behavior, every other temperature depended effect of components in the temperature-controlled chamber poses a systematic. The photo diode has a wavelength depended quantum efficiency. As the wavelength shifts during the measurement the quantum efficiency will change as well during the measurement. The calibration data for the diode is only given in a unclear plot and the calibration values have been sampled from the picture therefore can only be used for relative measurements.

In this case, as only the flasher and part of the fiber are placed in the freezer it is the fiber. Further testing has to be done to determine whether for example temperture related condansation changes the light coupling. Then the fiber mount itself to the module could be affected by thermal expansion and therefore affect the coupling.

This effect could be quantized by taking a measurement with a temperature controlled reference fiber. The plan was to connect a fiber to a temperature controlled LED flasher outside of the freezer and route it to the LED flasher in the freezer and connect it with a fiber adapter at its back. The fiber would connect to second mount on the back of the LED flasher and emit through a newly cut hole in the middle of the other LEDs. As we now have a light source a similar position but with constant intensity and a constant temperature, every measured divination must come from the fibers.

For the PMT the same effect is relevant to. It to has different quantum efficiency for different wavelength. Further more its efficiency is also dependent on the high voltage supplied by the amplifier. This might vary as well. The PMTs output will deviate from a linear correlation of voltage to intensity at higher intensities and even saturate at a certain point. In order to this and to protect the PMT from to high currents being created, it is automatically switched off if the output crosses a threshold set to 2 V.

For the angular isotropy measurement there is of course an uncertainty for the solid angle of the flasher. This might be of lesser significance during the absolute calibrated measurement as the dependence of the angle is some $\cos(\theta)$ law and therefore as little effect as long as uncertainties are small.

For the final absolute measurement, the same photo diode is used but a NIST calibrated one. This means the datasheet includes an extensive table of efficiencies and it is calibrated with an error of 0.02%.

For the picoamp it self has a dependent resolution of minimum of 0.2 ns for one connected channel, but only 0.4 ns for two and 0.8 ns for three as in our case. As we measure a time difference, this systematical error should accumulate. As in the analysis script the times are extrapolated, it should be somewhat better but as the signal of both devices is a square pulse it, should make little difference and the minimal resolution is probably around 1 ns. This is more than acceptable for qualitatively measuring the time profile and checking if the FWHM is under 10 ns but for an exact reconstruction one would have to improve this. Connecting only two signals, or both in one channel distinguishing them by software, taking vastly more samples. For the absolute timing there is of course a delay, connected to cable length etc. For the calibration this is of little concern, but later it has to be measured by the POCAM in-situ to provide the data to the flash reconstruction.

### 2.2.3 Measurements

For all of the following measurements the same default flasher has been used and only the LEDs have been swapped out. In total six LEDs have been tested. Therefore all LEDs should face the same systematics. Particular interest will lay on the characteristic of the XLR-400-5E which has proven reliable in the past [27] and with a wavelength of around 400 nm is well in the middle of the desired spectrum. The six tested LEDs are: MTE325H21-UV, MTE340H21-UV, XLR-400-5E, LED450-06, LED490-06 and LED570-03. As LEDs can differ dramatically dependent on the waver-batch, it is important to state that the here measured LED is from the a batch of 2019.

As a disclaimer, the following measurements are not actual calibration measurements for hardware that is going to be deployed. They have been conducted as a test for feasibility of the POCaS setup, as well as the selection of possible deployable LEDs with all desired properties. Furthermore, out of scientific curiosity it is tried to deduce if any of the in section 1.3.3 mentioned effects could explain the measured behavior of the LEDs. Temperature effects one the LEDs could not yet be measured as the freezer only became operational shortly and has not yet been implemented in the measurement setup. So the only changing parameter is the bias voltage which from herein on will be refer to as supply voltage as it is the only voltage that can be set and measured in the setup. It is reasonable to assume that the voltage is used to charge the Kapustinsky circuit and not drives the LED directly it is very close to the actual voltage present at the flasher board.

If not mentioned otherwise the voltage range for all measurements was from 5 V up to 30 V in 2.5 V-steps. 30 V has been selected as the current maximum, as from experience gained during these type of measurements it does not seem to be harmful to the flasher. Furthermore the laboratory power supply is only capable of outputting 32 V and as especially the UV LEDs can cost over a €100 a piece, no unnecessary gamble was taken.

#### 2.2.3.1 Aging

During the early stages of the POCaS development a default flasher has been continuously operated at 10 MHz over a period of a little over 160 h. This amounts to around 5.8 billion flashes. Far more than expected during the operational life span of the POCAM. Even though then was a slightly different transistor mounted in the Kapustinsky circuit, the results are comparable. An intensity measurement by the photo diode was take every six minutes. The averaged results can be seen in section 2.2.3.1.

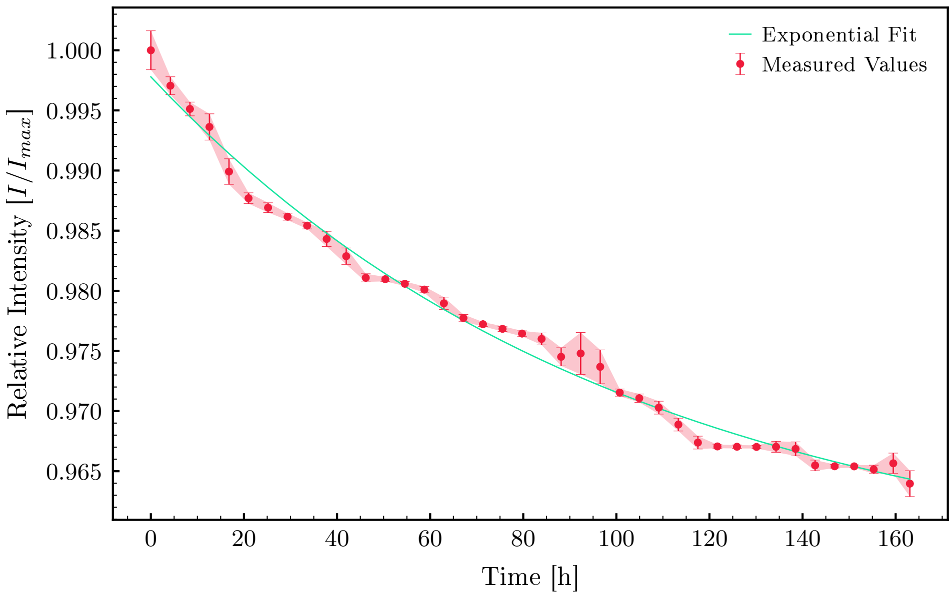


**Figure 2.5:** Relative drop in intensity of the default flasher with the 490 nm-LED. An exponential decline can be fitted to the measured values, with the total drop of intensity amounting to 4% over the course of 160 h continuous operation with 10 kHz

Ignoring the variation which are probable due to unmanaged systematics such as the fact that the dark box was not properly shielded against direct sun light, one can fit an exponential decline. Over the course of the measurement the relative intensity drop amounts to 4%.

#### 2.2.3.2 Intensity

As the intensity measurement is taken by two different devices, namely the photo diode and the PMT, the analysis of the data differentiates.

**In the photo diode measurement** this process is pretty straight forward, as only a current is measured by the picoamperemeter. It is set to automatically take 100 samples per measurement run. From these the average and standard distribution as statistical error is determined and plotted in section 2.2.3.2 below. As the standard distribution is extremely small the error bars are not visible. Even though the intensity measurement of the POCaS is not absolute as mentioned in section 2.1.3, the raw currents allow a comparison as the setups changes between measurements are small enough.

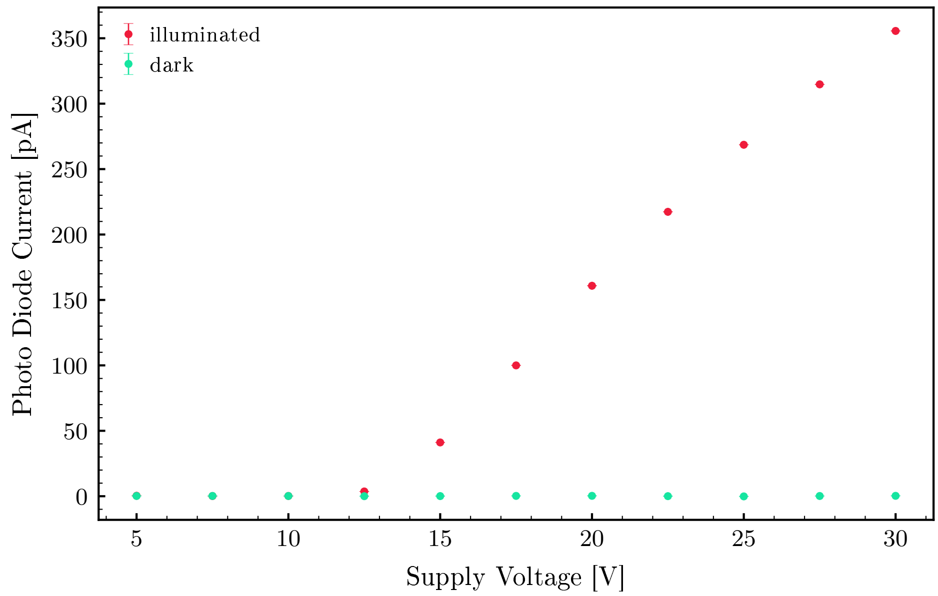


**Figure 2.6:** The measured photo diode current in picoampere at diffenent supply voltage of default flasher equipped with the default 400 nm LED. In green the dark current of the diode is plotted.

To estimate systematical errors the photo diodes dark current has been measured in between the individual voltage steps. It becomes apparent that the it is negligible with again a very small statistical error. This is a strong indication that dark box is sufficiently dark, although the PMT measurement has a higher light sensitivity and therefore is of greater importance to answer this question.

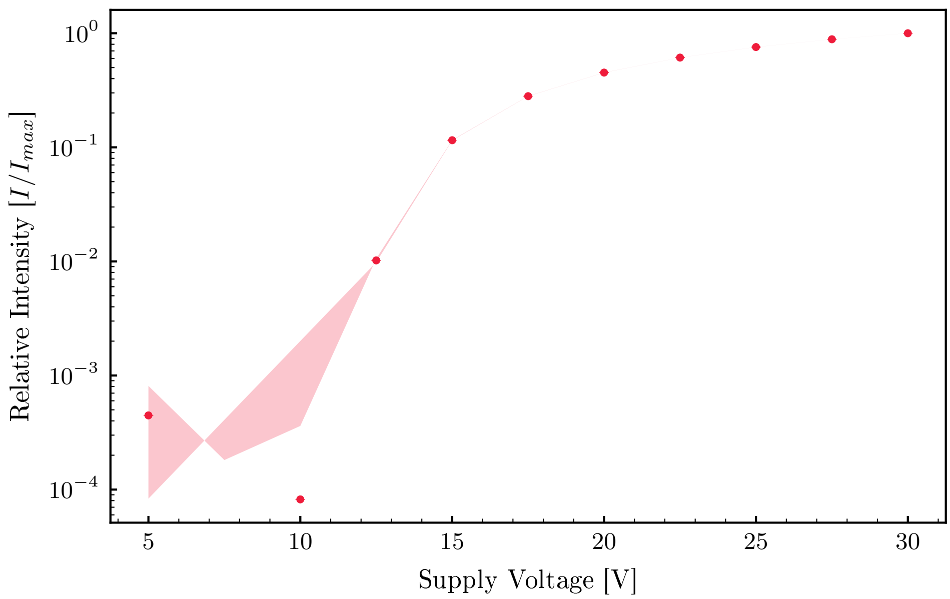


**Figure 2.7:** Relative intensity change with increasing supply voltages. The light production setting in between 12.5 V and 15 V.

As can be seen in section 2.2.3.2, the light production begins somewhere between 10 V and 12.5 V. A closer determination at this point is not possible as the voltage steps with 2.5 V are to wide. Even though a linear extrapolation might be tempting it does not give the desired result, as the actual correlation between supply voltage and LED intensity is a exponential function for low intensities and a logarithmic for high intensities. This is more apparent in section 2.2.3.2 where the scale is set to semi logarithmic. As especially for the default LED the wavelength shift is irrelevantly small, the light intensity is directly proportional to the diode current. By dividing all values by the highest one, the y axis represents a relative intensity. This clearly shows that there are almost four orders of magnitude between maximum and minimum illumination, an as soon as it produces light at 12.5 V the intensity jumps two orders of magnitude.

**The PMT measurement** is far more sensitive and can therefore be used to measure behavior at lower intensities. Being an analog device it is complicated to read out. Currently 100000 samples are taken per voltage step by the picoscope. As the intensity information lies in the pulse area a mean is fitted from all samples. This is accomplished by integrating the area under every peak, histograming these and fitting a Gaussian peak over the histogram, whose mean is the mean peak area. By dividing the value through the 50 Ω from the oscilloscope termination on arrives at the deposited charge plotted in fig. 2.8.

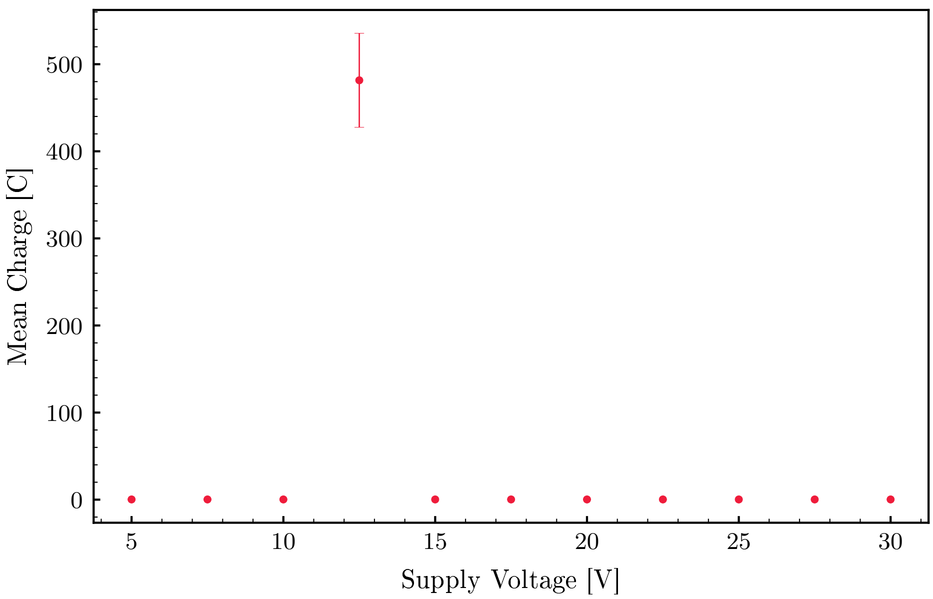


**Figure 2.8:** Intensity measurement by the PMT for the default LED. It is visible that the PMT only took one valid measurement before shutting off.

As there is no light up until 10 V as in the photo diode measurement, it seems that this LED does not yet flash at this point. Here two disadvantages of the PMT measurement become apparent: First if there is little to no light the mean fit fails as there is no clear peak shape and hence one gains no intensity information. Second it is only usable in a very small intensity range. The fact that there is no data after 12.5 V is due to the PMT is switching off if voltages higher than 2 V are measured at its output. This is to assure that the PMT is not damaged through high internal currents. To further establish the behavior at low intensities and to highlight the PMTs potential a measurement with 1 V-steps has been conducted for the 490 nm LED. The result can be seen in fig. 2.9.

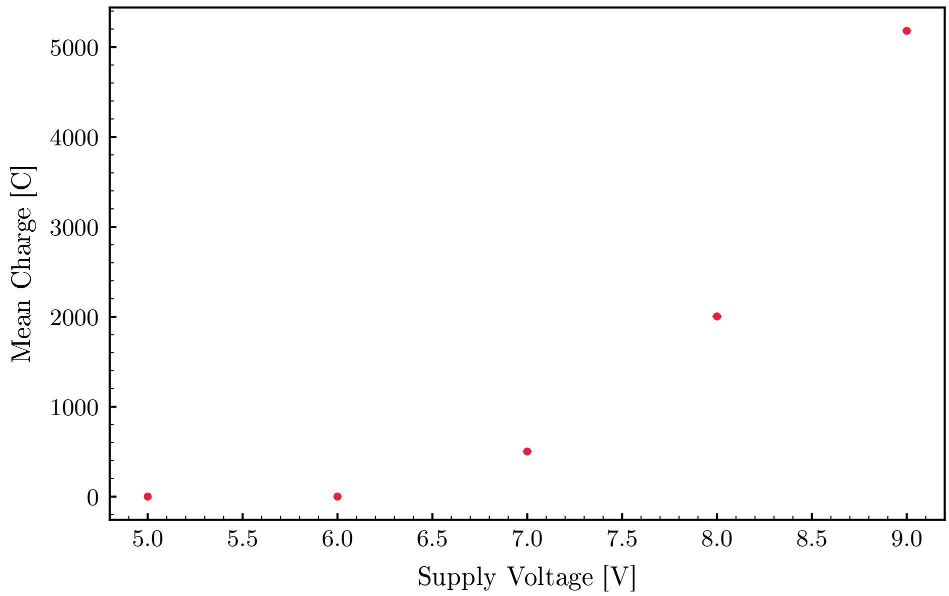


**Figure 2.9:** Intensity measurement of the 490 nm LED at a lower voltage range from 5 V to 10 V with one volt steps size.

Generally this 490 nm LED exhibits some unique characteristics in comparison to the other LEDs. Two of which can be seen in this measurement. First its really early onset of light production between a supply voltage of 6 V and 7 V. And second the high amount of light it produces. The default LED produces a charge approximately 500 C at its only measured value. This LED produces over 500 C of charge at 7 V.

This becomes even more apparent in the absolute current diode measurement.

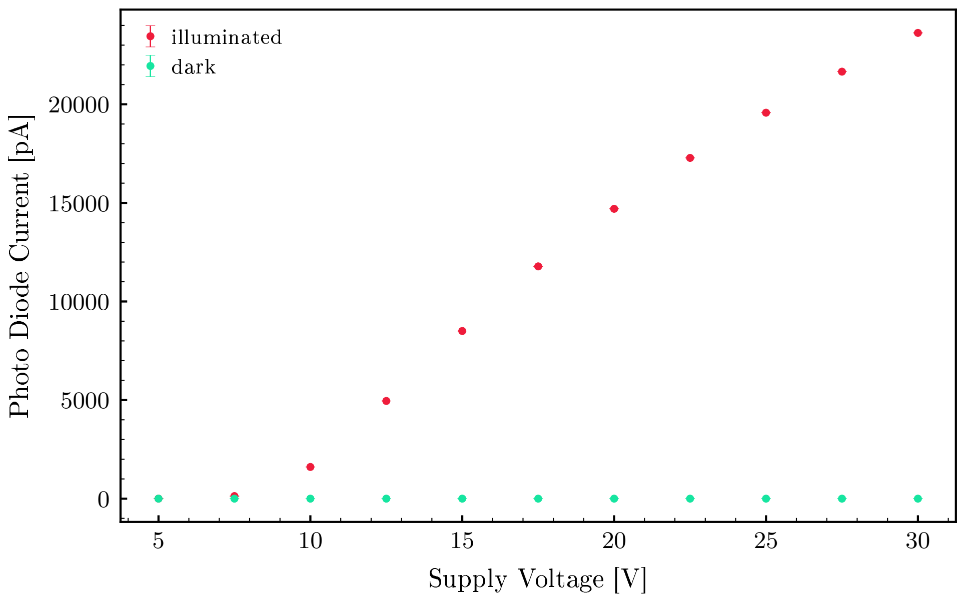


**Figure 2.10:** Absolute photo current measured dependent on the supply voltage. Illuminated and dark rate measurement are plotted separately. It is apparent that the dark current becomes negligible.

Here the current is almost two orders of magnitude higher than that of default LED. This cannot be explained solely through systematical uncertainties in for example fiber alignment.

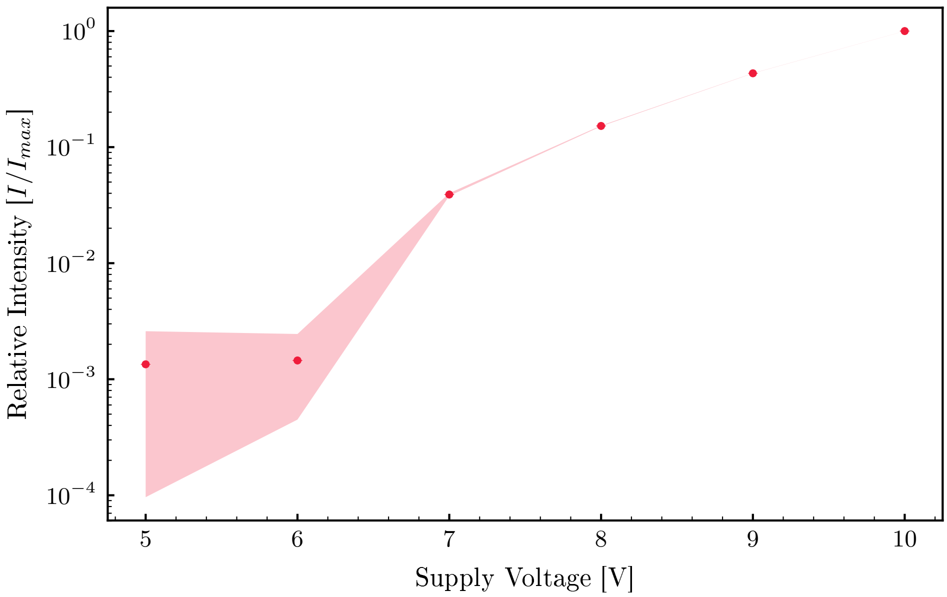


**Figure 2.11:** Logarithmic plot of the relative PMT intensities of the 490 nm LED at low voltages, with one volt intervals.

The behavior at low voltages seems to be exponential from the point of light emission onward. But at the edge of light no light emission to light emission seems to be a discontinuity. This could be due to the threshold voltage in p-n-junctions (compare section 1.3.2). Even tough this threshold voltage is normally close to the band gap energy, the short pulse and some parasitic capacitance in the LED could have the effect of shifting this threshold significantly.

**In Comparism** the two UV LEDs (325 nm and 340 nm) having a far later onset of light emission at around 15 V. Only the 450 nm and 570 nm LEDs have a similar emission onset between 7.5 V and 10 V as can be determined form section 2.2.3.2 and **??**. This would in deed support the theory that onset voltage is correlated with the threshold voltage of the diode. The 570 nm LED does not seem to follow this trend as closely, which might be due to a difference in semiconductor material.

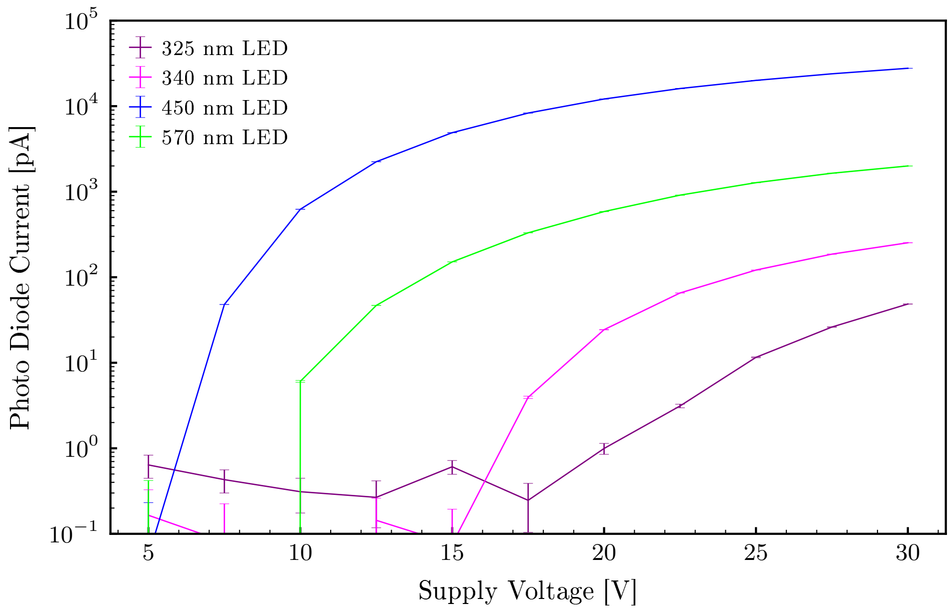


**Figure 2.12:** Logarithmic plot of the photo diode current of the 325 nm, 340 nm, 450 nm and 570 nm LEDs. One can clearly see the differences in onset of light production. The amount of current created is upto three orders of magnitude different depeding on the LED.

The differences in peak brightness between the different LEDs are orders of magnitude. Especially the UV LEDs have extremely low intensities measured by the photo diode. This might in part be contributed by the fact that each individual photon carries more energy, around 1.5 times more and a worst quantum efficiency of the photo diode wtih a factor 3 less than at 600 nm. Wavelength dependent coupling of the fiber may also play an important role. However these effects due not account for a three order of magnitude difference between the 325 nm LED and the 450 nm LED. Meaning that the effect has to be due to a difference in semiconductor material or the structure as UV LEDs use heterostructuring to form artificial quantum wells this might be far less efficient. further more it might just be that the UV LEDs need vastly more voltage to reach the same brightness, but as they are the most expensive ones it would be risky to test.

#### 2.2.3.3 Wavelength Shift

As mentioned in the section 2.2.2.1 the wavelength measurement works by taking a dark and illuminated measurement with the same integration time and subtracts them from each other. The resulting spectrum is then fitted with a Gaussian peak.

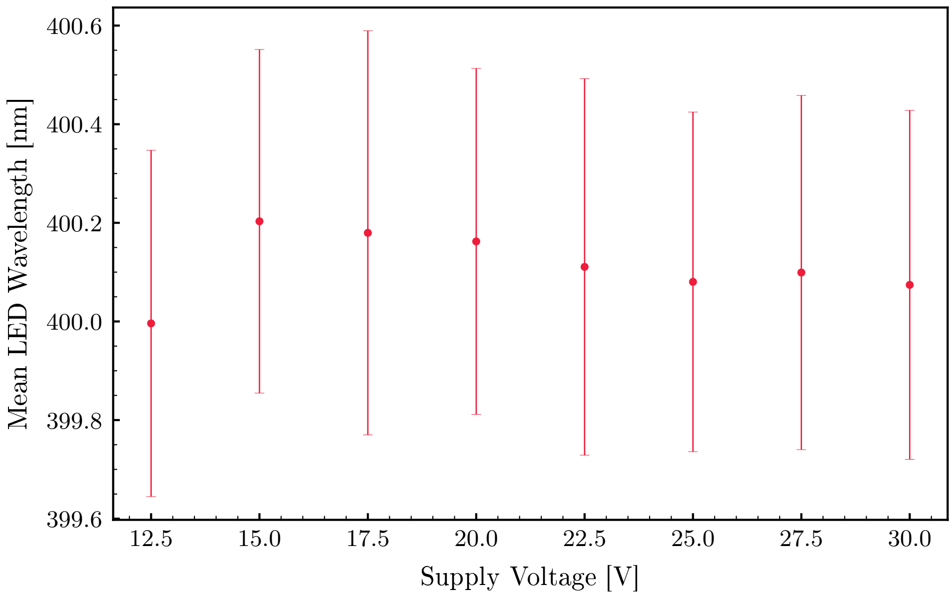


**Figure 2.13:** Mean LED wavelength of the default flasher dependent on the supply voltage.

For the default LED the mean wavelength is almost perfectly 400 nm over the entire voltage range. With the absolute shift being smaller than 1 nm and therefore within the reproducibility parameter of $\pm 0.5$ nm from the spectrometer.

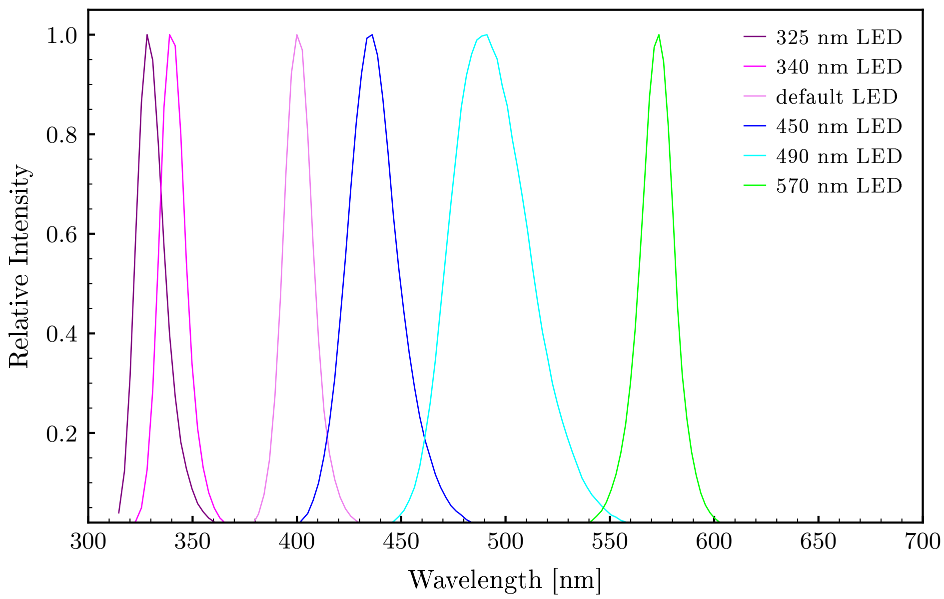


**Figure 2.14:** Normed spectra of all tested LEDs at 30 V.

As one can see in the section 2.2.3.3, the peaks are not entirely symmetrical and therefore not Gaussian shaped, but for the UV ranged LEDs in particular seems to have a tail towards longer wavelength. This could either be a semiconductor effect, due to impurity recombination with lower energies or due to a difference in quantum efficiency for different wavelength of the spectrometer. Impurity recombination could be seen in the pulse form, as impurity states have longer lifetimes and elongate the time profile. This and the fact that the tail portion of the peak seems to be independent from the supply voltage, strongly suggest that the tail is cased by a difference in quantum efficiency. As can be seen in figure 2.15, the quantum efficiency increases rapidly in the UV range meaning that such an effect would be most likely in this wavelength regime. That correlates well with the measured data.

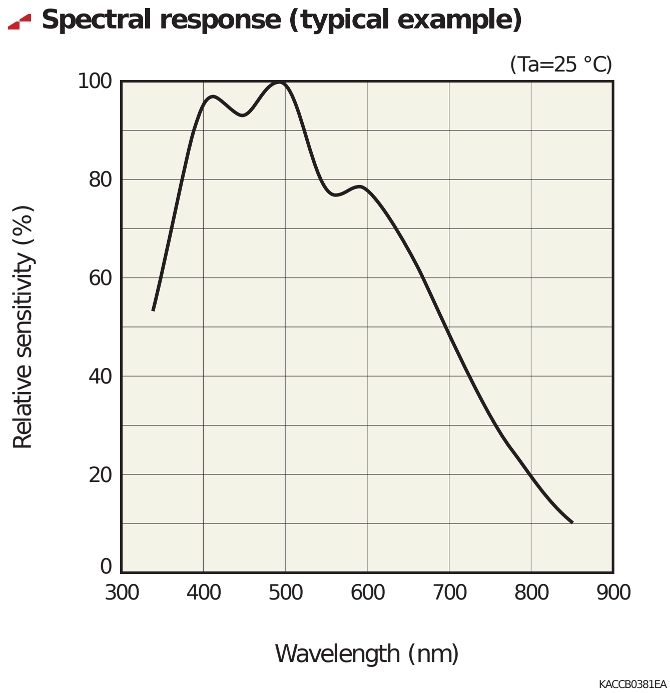


**Figure 2.15:** Relative wave sensitivity of the spectrometer. This might be an explanation for some of the pulse diverting from a Gaussian shape, but not for a shift in mean wavelength [26]

If the effect indeed is voltage independent it would equally shift the mean of all fitted Gaussian curves and therefore only account for an offset in the spectral shift measurement hence preserving it qualitative significance.

Similarly behaving is only the 340 nm LED with an even smaller absolute wavelength shift.

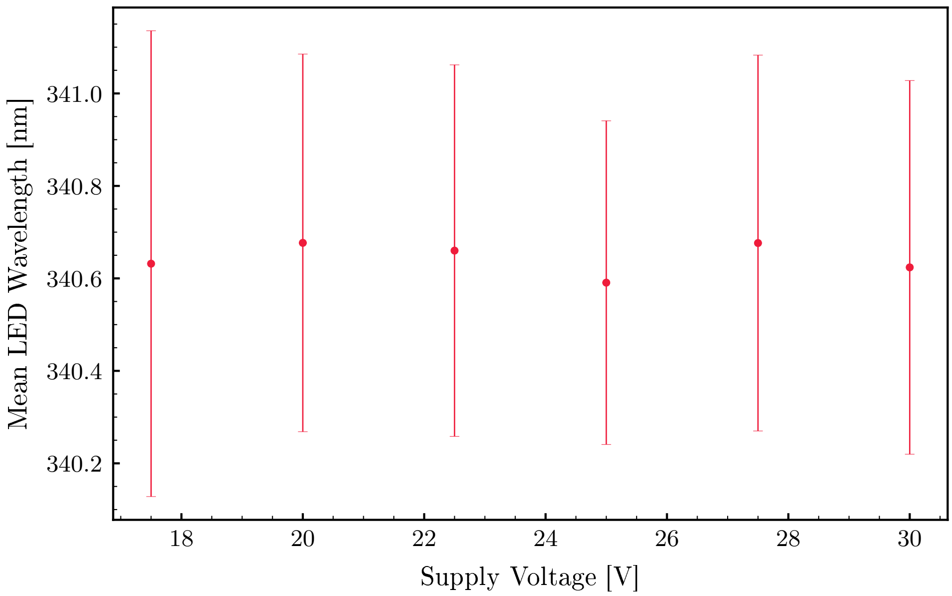


**Figure 2.16:** Wavelegnth shift of the 340 nm LED. This remains absolutely stable over the entire voltage range.

The following two LEDs, namely the 325 nm and 450 nm, all exhibit a shortening in wavelength with increased supply voltage. Although one can only speculate about the exact causes, one theory could be that with higher voltages more charge carriers are injected which at a certain point occupy all states close to the band edges and therefore transitions from states deeper in the bands become more likely. This would increase the energy of a fraction of the emitted photon and shift the spectrum. Another Theory is that at higher voltages an electric field is created in the semiconductor effectively increasing the band gap. With a drop of over 10 nm the effect of wavelength shift is most pronounced in the 450 nm LED.

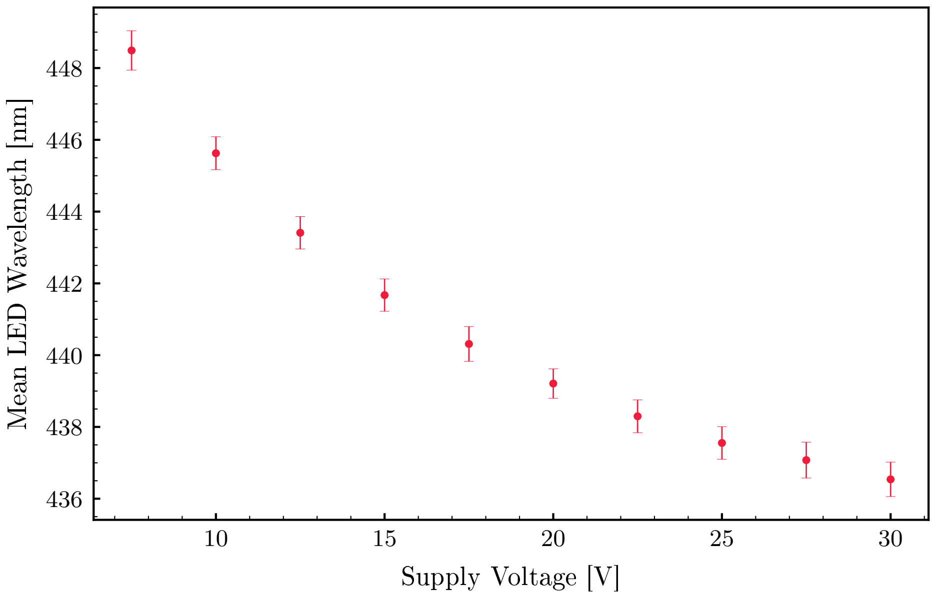


**Figure 2.17:** Mean wavelength shift of the 450 nm LED. It by far has the most significant shift of over 10 nm.

As can be seen in fig. 2.18 the trend is not as clear in the 325 nm LED. With a total drop in wavelength of around 1 nm it is actually still in the reproducebility uncertainty of the spectrometer, but the trend still seem visible in the same exponential manner as exhibited by the 450 nm LED.

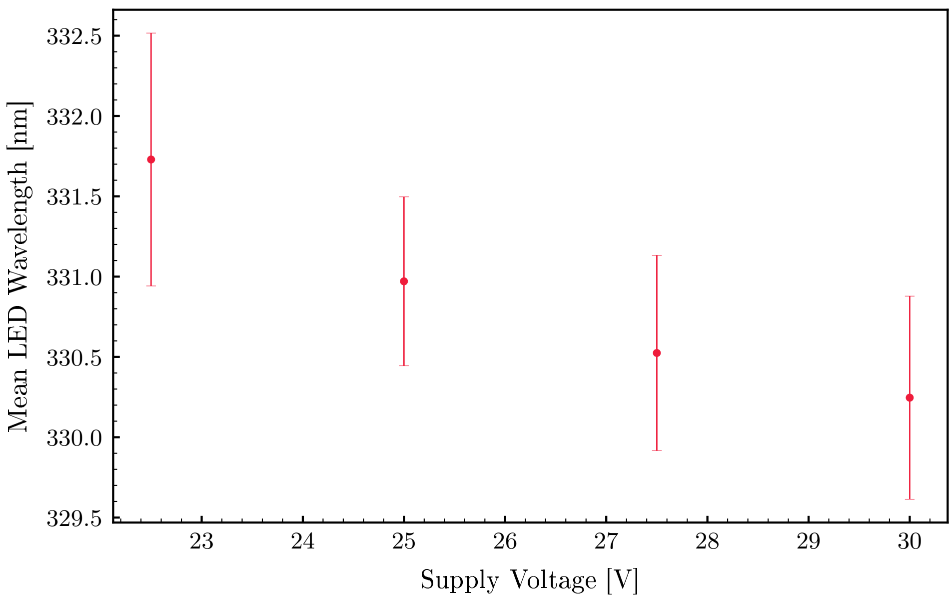


**Figure 2.18:** Mean wavelength shift of the 325 nm UV LED, with a overall decrease of 1 nm.

The 490 nm LED is the only one which exhibits a strong increase in wavelength between onset of light emission and 12.5 V, with a subsequent decrease of 5 nm meter toward higher voltages.

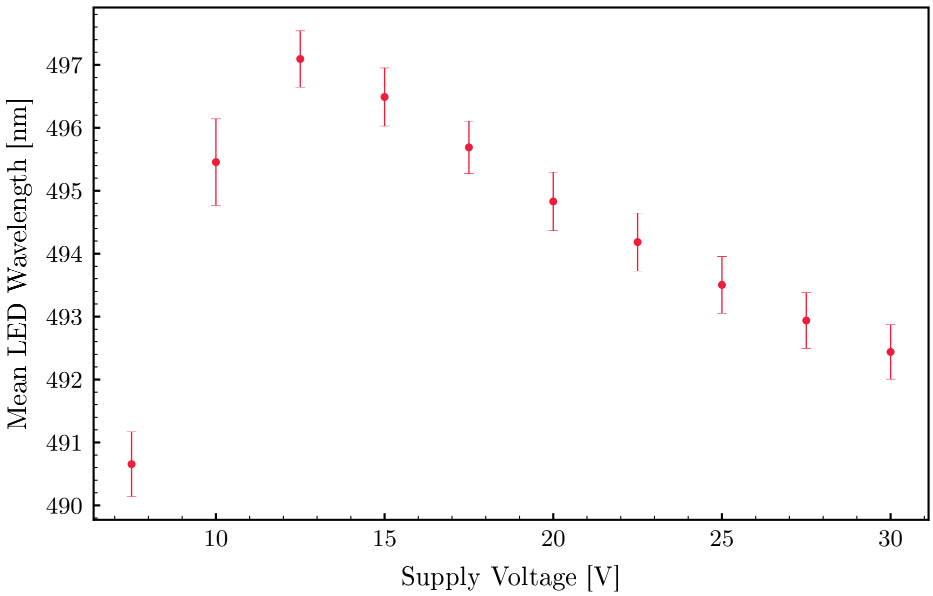


**Figure 2.19:** Mean wavelength shift of the 490 nm LED.

The unusual behavior of first rising wavelength and later on dropping, is due to the very broad spectrum peak which becomes with increasing voltage less Gaussian. The pulse becomes less symmetrical with a trail in the direction of higher wavelength. This is probably due to the impurity transitions which increasingly get populated. This can also be seen in the time profile of this LED.

The last LED tested was the 570 nm LED. Its absolute wavelength shift is less then a nanometer, further more the quantum efficiency of the spectrometer in the 500 nm to 600 nm range is quiet variable and has a local minimum just around 570 nm therefore the shift could very well be caused solely by systematical errors of the spectrometer.

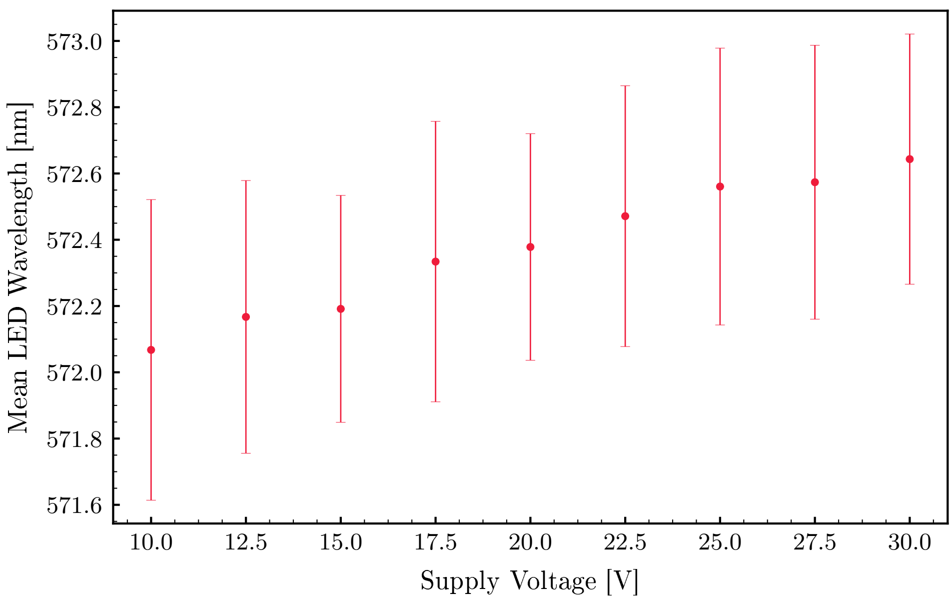


**Figure 2.20:** Mean wavelength shift of the 570 nm LED. One can clearly observe an increase

#### 2.2.3.4 Time Profile

The time profile is measured by time correlated single photon counting, as described in section 2.2.2. The measured time difference between the extrapolated rising edge of trigger signal in one channel of the picoscope and the APD pulse in another channel, is histogamized to represent the pulse form. The resulting resolution is dependent on the bin size. As there are only a fixed number of measured time differences the amount of counts per bin decrease if bin size is decreased. Another limiting factor is the time resolution of the picoscope which is set to minimum value of 0.8 nm for the case of three sampled inputs (Trigger, APD, PMT). For all following measurement for every voltage step $10^5$ trigger pulses have been recorded. As the occupancy between promille and a few percent with 10% being the allowed maximum, the number of recorded time differences varies vastly with LED intensities and selected attenuation filter.

For the default LED the time profiles at 12.5 V, 15 V and 30 V are plotted in fig. 2.21. Here two characteristics are worth mentioning, first the shift of arrival times and second the broadening of the profile at higher supply voltages. The amount and the direction of the shift of arrival times varies greatly between the LEDs with the default LED being the only one exhibiting such a clear increase with increasing supply voltage. The second effect seems to be more universal. This might suggest that the broadening is caused either by the kapustinsky circuit itself, a universal phenomenon of LEDs, like the parasitic capacitance, or a combination of both.

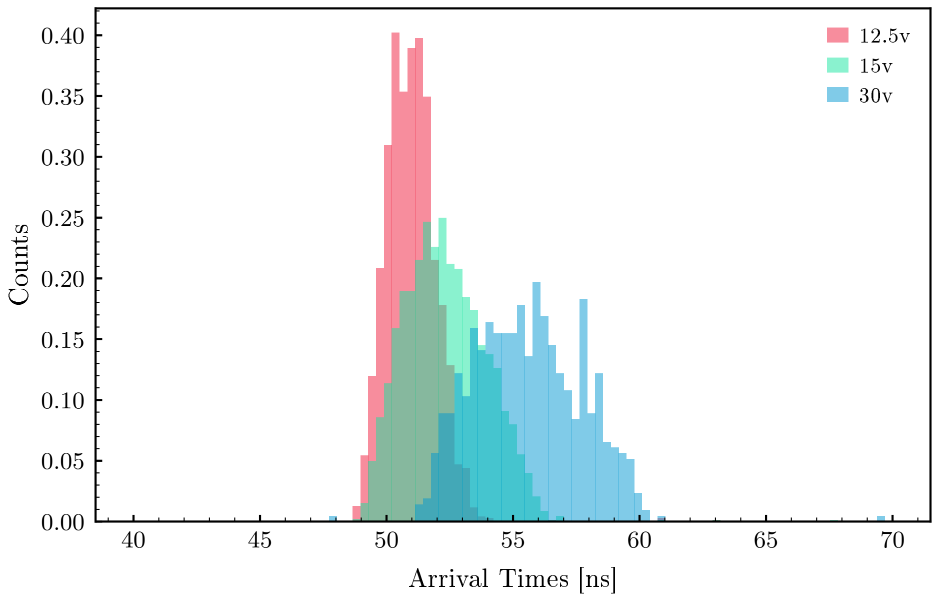


**Figure 2.21:** Time profiles of the default LED at 12.5 V, 15 V and 30 V

Further more all time profiles of the default LED are shorter then 10 ns in total thus being well within the parameter specified for the POCAM.

As the intensity of the 325 nm LED was generally very low, the occupancy is aswell which makes for a low number of counts per bin. Hence the resulting time profiles are not as clear, as can be seen in fig. 2.22. Nevertheless it seems that in this case arrival times are decreasing with increasing supply voltage. As the time profiles are taken at successive voltage steps, the broadening effect can not be clearly observed and might just be an optical illusion as count numbers per bin rise and the pulses become more refined.

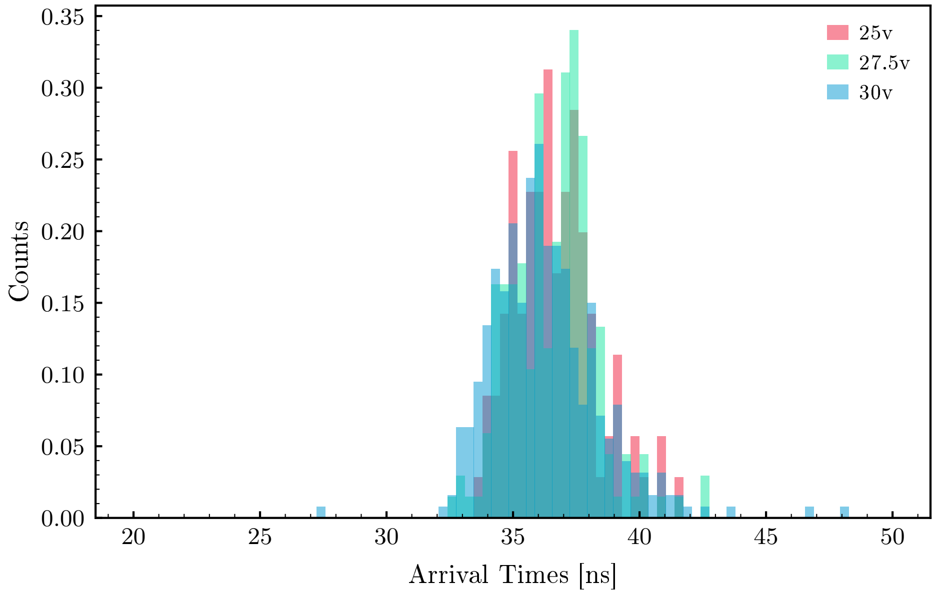


**Figure 2.22:** Time profiles of the 325 nm UV LED at 25 V, 27.5 V and 30 V

In section 2.2.3.2 it was already established that the 340 nm UV LED is significantly brighter then the 325 nm one. Therefore the occupancy improved as well and the measured time profiles are better refined. Now a clear shift towards lower arrival times is visible. Especially between the 20 V and the 30 V profile a broadening of the pulse becomes apparent.

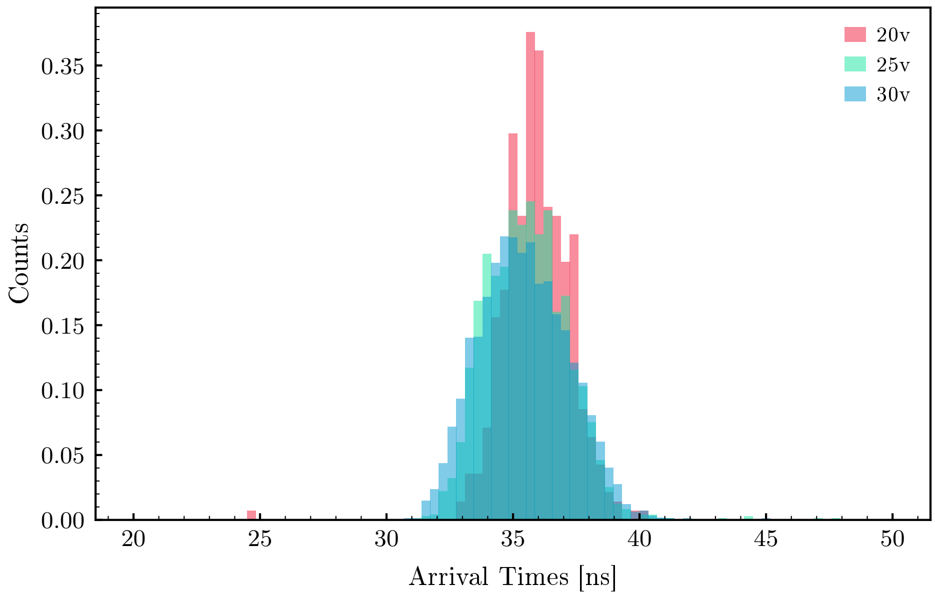


**Figure 2.23:** Time profiles of the 340 nm UV LED at 12.5 V, 15 V and 30 V

Both UV LEDs have a total peak width of under 10 nm and therefore produce sufficiently sharp pulses. Something that is not the case for 450 nm LED. Its total pulse length is 20 ns for all measured voltages of 15 V, 22.5 V and 30 V. Furthermore this LED's time profile seems to be completely independent of the supply voltage. This fact might make the LED still suited for deployment in the POCAM, especially as it produces very high intensities.

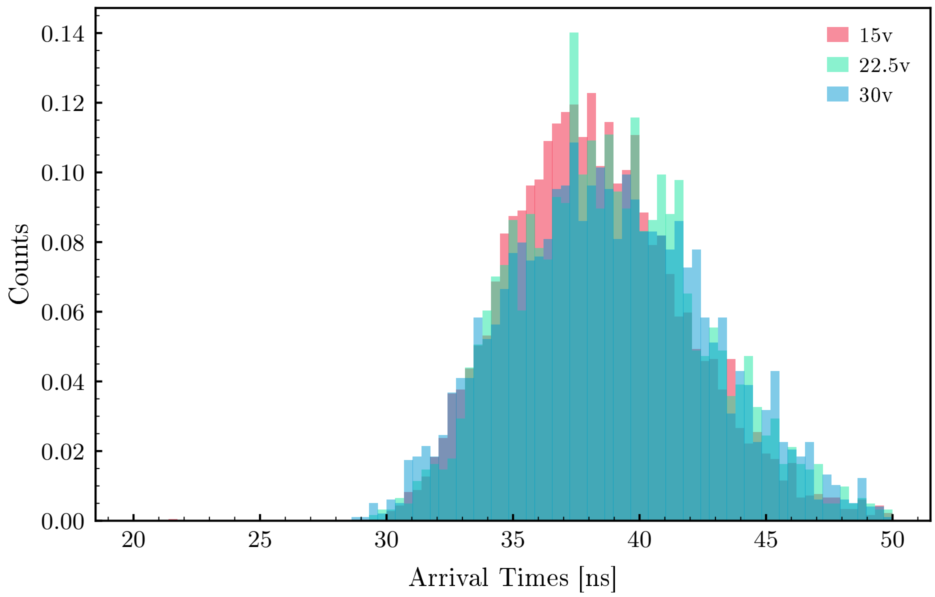


**Figure 2.24:** Time profiles of the 450 nm LED at 15 V, 22.5 V and 30 V

The time profile of the 490 nm LED has been plotted at three successive voltages, therefore not much variation between them can be seen. The most noticeable feature however is the long tail after the initial peak, making the total profile at least over 100 ns long. As the binning range ends at 150 ns the complete profile has not been recorded. This long illumination period makes this LED unusable in the POCAM flasher.

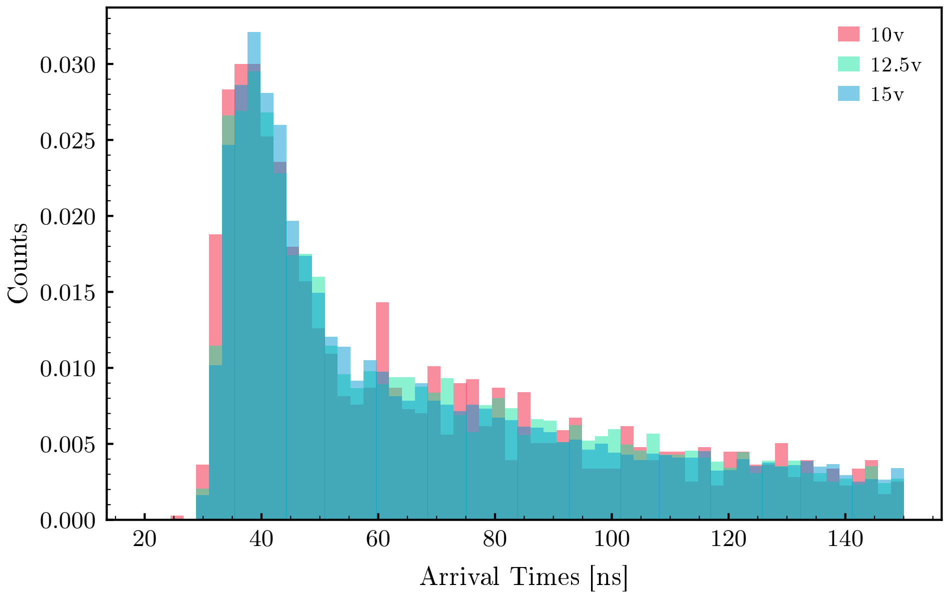


**Figure 2.25:** Time profiles of the 490 nm LED at 10 V, 12.5 V and 15 V

The tail of the profile looks like a slow exponential decline which would suggest a long lived state transitions as the root of the emitted light. Normally impurities would be a prime candidate for this effect, as they can trap holes and electrons and therefore constrain there energy. Due to Heisenbergs uncertainty principle the time uncertainty increases when energy uncertainty increases, therefore impurity states are long lived. In most materials this only decreases the efficiency of the LED as theses states recombine non-radiatively.

This however is not the case in Indium gallium nitride (InGaN), which is very likely the material chosen for this LED. To achieve 490 nm emission wavelength a medium ratio of Indium to gallium is used. As especially gallium nitride is prone to forming crystal defects, indium rich regions occur. These can, similar to impurities, trap electron hole pairs but the recombination is radaitively [28]. Therefore creating a delayed tail of photon emission. As the indium rich regions also have a smaller band gap it might also be the reason for the initial increase in wavelength as seen in fig. 2.19.

The fact that this effect is not as pronounced in the 450 nm LED even though it is InGaN aswell (or Zinc Selenide in which case this is irrelevant) due to effect that is has a far smaller ratio of indium to gallium in order to modulate the band gap to 450 nm transitions.

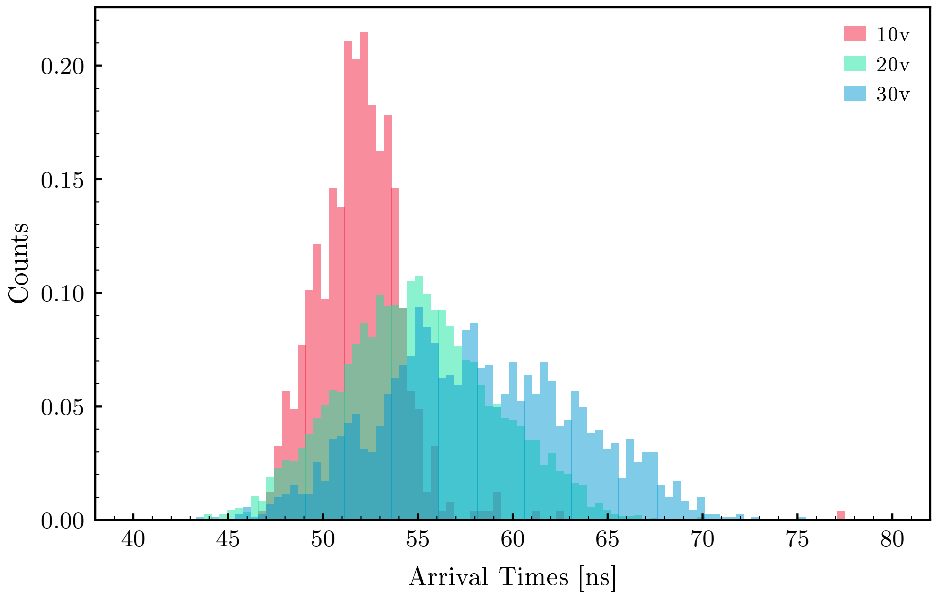


**Figure 2.26:** Time profiles of the 570 nm LED at 10 V, 20 V and 30 V

The 570 nm LED behaves very similar to the default LED, but generally has longer pulses upto 25 ns. Also there is no clear shift of arrival times to identify.

## 2.3 Conclusion

As the motivation for this thesis was to streamline the future calibration of POCAM flasher through fully-automated calibration station. The following aspects are considered in the evaluation of the conducted measurements: First was the measurement successful in delivering usable calibration data. Second, what degree of automation has been achieved. Third was it possible to use the data to reject or embrace the tested LEDs for a possible deployment.

The individual measurements where all able to achieve sufficiently high resolution to be able to observe changes in the LEDs characteristics with increasing supply voltages. If the data quality is high enough to satisfy the demands of the IceCube Collaboration will be discussed in upcoming meetings in October.

Furthermore a the automation of the setup is so far progressed that after mounting the to be tested LED on the flasher board and connecting is to the voltage supply, the trigger signal and the fiber adapter in the dark box, one simple sets the voltage range in the measurement script and executes it. All instruments then take data at every voltage step automatically. Typical runs in the current setup take around 20 minutes, after that all measured data is saved into a folder.

The narrowing down of the selection of possible LEDs for deployment in the POCAM could also be achieved. As the default 405 nm LED has been preselected from the start the it was good to see that results of previous measurements could be reproduced and therefore act as a sanity check for the whole setup. The LED was definitely within the specifications for deployment with a pulse duration under 10 ns throughout the voltage range. No significant wavelength shift was measured and its intensity being in the medium range as well as its threshold for light production. The fact that it is not as bright as other LEDs is not necessarily a disadvantage as brighter LEDs all seem to exhibit some form of unwanted behavior. Either a significantly longer pulse duration or a more extreme wavelength shift.

The two UV LEDs both had sufficiently shot pulses and little to no wavelength shift has been measured. The main drawback is that both have low measured intensities. This might be in part due to the lower sensitivity for UV wavelength of the setup meaning the 340 nm LED might actually be comparably bright as the default LED. But the 325 nm LEDs low brightness can not be explained through this effect alone. As the POCaS is only designed for relative intensity measurement, the final decision has to be made after the absolute intensity measurement with the NIST calibrated photo diode. The 340 nm LED on the other hand might be a suited candidate for deployment.

The decision for the 450 nm LED is equally unclear, on the one hand it was the brightest LED in the test and its pulse profile is unaffected by changing supply voltages. On the other hand with is with around 20 ns somewhat broader and its mean wavelength shifts by over 10 nm.

A clear decision can be made with the 490 nm LED as is elongated time profile, which is most probably due to radiatively recombining impurities makes it unusable in the POCAM. For the 570 nm LED it is also difficult to make a decision, as its pulse length increases substantially with increasing supply voltage. Here one would be well advised to compare it to other LEDs with a similar wavelengths.

What are the next steps from here In the near future the freezer will be incorporated into the measurement to characterize the behavior for changing temperatures as well. Then the setup has to be further tested for temperature related systematics. If it is determined that temperature related effect in the fibers are to pronounced the possibility to include a temperature stabilized reference flasher exists.

If it is determined that some systematics are to large for IceCube purposes, there are a few thoughts onto further eliminating the systematics: Further systematics can be reduced by using only on channel of the picoscope and distinguishing the pulses by software. This would increase the resolution 0.2 ns in the time profile measurement.

For the wavelength shift the closer determination of quantum efficiency of the spectrometer by measuring the response to 1 nm-FWHM spectral filters is in planning. Also decreasing voltage step size and increasing the amount of samples taken by the picoscope will also increase the precision of the measurement results at the cost of longer measurement times.

# Bibliography


[1] Bogdan Povh et al. *Teilchen und Kerne*. 2014. ISBN: 978-3-642-37822-5. DOI: https://doi.org/10.1007/978-3-642-37822-5.

[2] Susanne Mertens. 'Direct Neutrino Mass Experiments'. In: *Journal of Physics: Conference Series* 718 (May 2016), p. 022013. DOI: 10.1088/1742-6596/718/2/022013. URL: https://doi.org/10.1088%2F1742-6596%2F718%2F2%2F022013.

[3] MG Aartsen et al. 'Measurement of South Pole ice transparency with the IceCube LED calibration system'. In: *Nuclear Instruments and Methods in Physics Research Section A: Accelerators, Spectrometers, Detectors and Associated Equipment* 711 (2013), pp. 73–89.

[4] F. Reines et al. 'Detection of the Free Antineutrino'. In: *Phys. Rev.* 117 (1 Jan. 1960), pp. 159–173. DOI: 10.1103/PhysRev.117.159. URL: https://link.aps.org/doi/10.1103/PhysRev.117.159.

[5] M. G. Aartsen et al. 'A COMBINED MAXIMUM-LIKELIHOOD ANALYSIS OF THE HIGH-ENERGY ASTROPHYSICAL NEUTRINO FLUX MEASURED WITH ICECUBE'. In: *The Astrophysical Journal* 809.1 (Aug. 2015), p. 98. DOI: 10.1088/0004-637x/809/1/98. URL: https://doi.org/10.1088%2F0004-637x%2F809%2F1%2F98.

[6] W. David Arnett et al. 'Supernova 1987A'. In: *Annual Review of Astronomy and Astrophysics* 27.1 (1989), pp. 629–700. DOI: 10.1146/annurev.aa.27.090189.003213. eprint: https://doi.org/10.1146/annurev.aa.27.090189.003213. URL: https://doi.org/10.1146/annurev.aa.27.090189.003213.

[7] P Padovani et al. 'Dissecting the region around IceCube-170922A: the blazar TXS 0506+ 056 as the first cosmic neutrino source'. In: *Monthly Notices of the Royal Astronomical Society* 480.1 (2018), pp. 192–203.

[8] Howard Haber. *The power spectrum of Cherenkov radiation*. University of California, Santa Cruz. URL: http://scipp.ucsc.edu/~haber/ph214/cherenkov17.pdf.

[9] Felix Henningsen. 'Optical Characterization of the Deep Pacic Ocean: Development of an Optical Sensor Array for a Future Neutrino Telescope'. In: (), p. 102. URL: http://www.cosmic-particles.ph.tum.de/fileadmin/w00bkl/www/Thesis/Master_Thesis_compressed.pdf.

[10] Francis Halzen. Department of Physics, University of Wisconsin, CC BY 3.0, URL: https://commons.wikimedia.org/w/index.php?curid=26350372.

[11] Francis Halzen. 'The AMANDA neutrino telescope'. In: *Progress in Particle and Nuclear Physics* 40 (1998), pp. 377–390.

[12] Rasha Abbasi et al. 'Calibration and characterization of the IceCube photomultiplier tube'. In: *Nuclear Instruments and Methods in Physics Research Section A: Accelerators, Spectrometers, Detectors and Associated Equipment* 618.1-3 (2010), pp. 139–152.

[13] Martin Rongen Kai Krings Elisa Resconi. 'The Precision Optical CAlibration Module forIceCube-Gen2: First Prototype'. In: URL: https://pos.sissa.it/301/934/pdf.

[14] Aya Ishihara. 'The IceCube Upgrade–Design and Science Goals'. In: *arXiv preprint arXiv:1908.09441* (2019).

[15] Christian Fruck, Felix Henningsen and Christian Spannfellner. 'The POCAM as self-calibrating light source for theIceCube Upgrade'. In: *36th International Cosmic Ray Conference (ICRC 2019) Madison, Wisconsin, USA, July 24-August 1, 2019*. 2019. eprint: 1908.09600.

[16] B. Van Zeghbroeck. *Energy bands*. 2011. URL: https://ecee.colorado.edu/~bart/book/book/chapter2/ch2_3.htm (visited on 03/09/2019).

[17] F. Reif. *Fundamentals of Statistical and Thermal Physics*. Waveland Press, 2009. ISBN: 9781478610052. URL: https://books.google.de/books?id=ObsbAAAAQBAJ.

[18] S.M. Sze and K.K. Ng. *Physics of Semiconductor Devices*. Wiley, 2006. ISBN: 9780470068304. URL: https://books.google.de/books?id=o4unkmHBHb8C.

[19] E.F. Schubert. *Light-Emitting Diodes (3rd Edition)*. E. Fred Schubert, 2018. ISBN: 9780986382666. URL: https://books.google.de/books?id=GEFKDwAAQBAJ.

[20] MG Aartsen et al. 'The IceCube Neutrino Observatory: instrumentation and online systems'. In: *Journal of Instrumentation* 12.03 (2017), P03012.

[21] Christian Spannfellner. 'Optical Characterization of the Deep Pacic Ocean: Development of an Optical Sensor Array for a Future Neutrino Telescope'. In: (), p. 62. URL: http://www.cosmic-particles.ph.tum.de/fileadmin/w00bkl/www/Thesis/Master_Thesis_compressed.pdf.

[22] Martin Rongen and Merlin Schaufel. 'Design and evaluation of a versatile picosecond light pulser'. In: *Journal of Instrumentation* 13.06 (2018), P06002.

[23] *Photomultiplier tubeR1925A*. URL: https://www.hamamatsu.com/eu/en/product/type/R1925A/index.html.

[24] *ID100 Visible Single-Photon Detector*. URL: https://marketing.idquantique.com/acton/attachment/11868/f-0236/1/-/-/-/-/ID100_Brochure.pdf.

[25] *S2281 series silicon photodiode*. URL: https://www.hamamatsu.com/resources/pdf/ssd/s2281_series_kspd1044e.pdf.

[26] *Mini-spectrometer C12880MA*. URL: https://www.hamamatsu.com/resources/pdf/ssd/c12880ma_kacc1226e.pdf.

[27] Felix Henningsen. 'STRAW (STRings for Absorption length in Water): pathfinder for a neutrino telescope in the deep Pacific Ocean'. In: *EPJ Web Conf.* Vol. 207. 2019, p. 06006.

[28] Fabio Sacconi, Matthias Auf der Maur and Aldo Di Carlo. 'Optoelectronic properties of nanocolumn InGaN/GaN LEDs'. In: *IEEE Transactions on Electron Devices* 59 (Nov. 2012), pp. 2979–2987. DOI: 10.1109/TED.2012.2210897.